X-ray diffraction study of strain-induced crystallization of hydrogenated nitrile-butadiene rubbers: Effect of crosslink density

Giuseppe Femina, Odda Ruiz de Ballesteros, Gaia Urciuoli, Martin van Duin, Christoph Gögelein, Daniele Tammaro, Paul Sotta, Finizia Auriemma

X-Ray Diffraction Study of Strain-Induced Crystallization of Hydrogenated Nitrile-Butadiene Rubbers: Effect of Crosslink Density

Giuseppe Femina,[†] Odda Ruiz de Ballesteros,[†,] Gaia Urciuoli,[†] Martin van Duin,[§] Christoph Gögelein,[%] Daniele Tammaro,[‡] Paul Sotta,[#] Finizia Auriemma[†,*]*

[†]Dipartimento di Scienze Chimiche Università di Napoli Federico II, Complesso Monte S. Angelo, Via Cintia, I-80126 Napoli, Italy

[§]Arlanxeo Netherlands B.V., P.O. Box 1130, 6160 BC Geleen, The Netherlands

[%]Arlanxeo Deutschland GmbH, Kaiser-Wilhelm-Allee 40, 51369 Leverkusen, Germany

[‡]Dipartimento di Ingegneria Chimica, dei Materiali e della Produzione Industriale, University of Naples Federico II, P. le Tecchio 80, 80125, Napoli, Italy

[#] Ingénierie des Matériaux Polymères, Université de Lyon, CNRS, UMR 5223, Université Lyon 1, INSA Lyon, Université Jean Monnet, F-69621 Villeurbanne cedex, France

*To whom correspondence should be addressed: Telephone: ++39 081 674443; e-mail: finizia.auriemma@unina.it; Telephone: ++39 081 674448; e-mail: odda.ruizdeballesteros@unina.it

Key words: Specialty elastomers; Strain induced crystallization (SIC); Orientation of the amorphous phases; SIC rate; WAXS analysis.

Abstract.

The structure and the mechanical and thermal properties of a hydrogenated acrylonitrile-butadiene rubber (HNBR) with acrylonitrile content of 44 wt% and residual unsaturation content of 9 % are investigated as a function of the crosslink density. The analysis is focused on specimens that have not been subjected to

any prior deformation. All samples are amorphous at room temperature and show glass transition temperatures that increase with increasing crosslink density. The values of the Young's modulus of the vulcanized samples are three times higher than that of the non-vulcanized counterpart and tend to increase with increasing the crosslink density. The tensile strength increases with increasing crosslink density, whereas the deformation at break decreases. All samples are amorphous at low deformations and whereas the non-vulcanized and the weakly and medium crosslinked samples undergo strain-induced crystallization (SIC) above a critical value of deformation, the highly crosslinked samples show only faint SIC and rupture at deformations slightly higher than that at SIC onset. It is shown that the deformation at SIC onset for the crosslinked samples tends to increase with increasing the crosslink density. This is in contrast with the prediction of Flory's theory for a homogeneous network. Instead, in agreement with Flory's predictions, the degree of orientation of the amorphous phase, increases with increasing deformation and reaches a plateau at SIC onset, indicating that the onset of crystallization is associated with a relaxation of the amorphous chains connected to the crystalline stems. The remarkable tensile strength of the crystallizing HNBR samples at high deformations is attributed to the strong alignment of the crystals in the stretching direction formed by SIC, causing pronounced strain hardening.

Introduction.

Hydrogenated acrylonitrile-butadiene rubbers (HNBRs) with acrylonitrile (ACN) contents ranging from 17 to 50 wt% are polar elastomers, produced by controlled and selective hydrogenation of the -C=C- unsaturation of acrylonitrile-butadiene rubbers (NBRs). Typically, elastomers characterized by fully or partially saturated polymer chains, with residual unsaturation contents between 0.9 and 9%, are produced [1],[2], which can be crosslinked with either peroxides or sulfur vulcanizing systems. HNBRs combine the outstanding resistance to oil and aggressive chemicals typical of NBRs, with the resistance to ozone, ultra-violet radiation, sour gas and high temperatures that characterizes main-chain saturated elastomers, such as ethylene-propylene-diene rubbers [3]. HNBRs are specialty rubbers with important applications in the automotive and aerospace industries, as they are well suited materials for rubber timing belts, hoses, sealing valves, vibration dampers and many other applications [3], [4], [5], [6], [7], [8].

The microstructure of the HNBR chains is complex, as it includes (i) hydrogenated *cis*- and *trans*-1-4-butadiene units, that give rise to tetramethylene sequences; (ii) a small amount of 1,2-butadiene units, that are fully hydrogenated, because of the high reactivity of the lateral double bonds; (iii) residual *cis*- and *trans*- 1,4-butadiene unsaturation, the content of which depends on hydrogenation conditions [2], [8]; (iv) ACN units.

Properties, such as the glass transition temperature, mechanical strength, oil resistance of HNBR systems are strongly dependent on the ACN content [7]. In particular, the high mechanical strength achieved by HNBRs at large deformations is generally ascribed to the crystallization of long, regular constitutional sequences induced by strain, *i.e.* strain-induced crystallization, SIC, and is critically dependent on the ACN content [7], [9], [10], [11]. X-ray scattering measurements at room temperature (*RT*) have shown that peroxide-vulcanized rubbers with ACN contents equal to or lower than 36 wt% undergo SIC due to the crystallization of the tetramethylene sequences in the orthorhombic or pseudo-hexagonal form of polyethylene (PE) [1], [10], [11], [12]. For networks with ACN contents higher than ≈39 wt%, instead, SIC is due to the crystallization of sequences of tetramethylene units regularly alternating with ACN units (TMAC) [1], [10], [11], [13].

The orientation of chain segments and SIC behavior of peroxide-crosslinked HNBRs with ACN contents of 19, 33, 41 and 44 wt%, residual unsaturation contents of 5% and similar crosslink densities have been recently investigated by using polarized Fourier Transform Infrared spectroscopy and synchrotron radiation wide-angle X-ray diffraction [11]. It was shown that, in accord with the previous studies [1], [10], [13], the samples with 19, 41 and 44 wt% of ACN showed SIC. In particular, the sample with the ACN content of 19 wt% started crystallizing at 200% deformation and achieved the highest level of crystallinity, forming well-oriented crystals. The samples with ACN contents of 41 and 44 wt% started crystallizing at 400 and 300% deformation, respectively, and although the degrees of crystallinity were lower than that of the sample with 19 wt% ACN, they reached a higher degree of crystal orientation with the chain axis parallel to the stretching direction [11]. It was shown that, at deformations greater than the deformation marking the SIC onset, the sample with 44 wt% ACN achieved stress values higher than

those achieved by the samples with lower ACN contents, and also the increase of the orientation of the chains in the crystalline and amorphous phases and of crystallinity was steeper [11].

So far, the SIC behavior of crosslinked rubber networks has been extensively studied for natural rubber (NR). These studies have highlighted that the characteristic features of SIC are: i) the orientation of the amorphous phase along the stretching direction before crystallization; ii) the consequent decrease of the crystallization entropy; iii) the formation of well-oriented crystals along the stretching direction; iv) the consequent partial recovery of conformational entropy due to the partial relaxation of the amorphous chains [14], [15]. The anisotropy in the orientation of the segments belonging to the crystalline and amorphous phases induced by stretching, gives rise to X-ray fiber diffraction patterns characterized by an anisotropic intensity distribution in the two-dimensional patterns from both phases [16]. The anisotropy of the diffraction halo from the amorphous chains has been interpreted according to distinct views [17], [18], [19], [20], [21], [22], [23], [24], [25], [26] [27], [28], [29], [30], [31]. On the one hand, it is suggested that this anisotropy is due to the contribution from an oriented amorphous phase overlaying a contribution from an unoriented amorphous phase [17], [18], [19], [20], [21], [22], [23], [24]. On the other hand, only one kind of weakly oriented amorphous phase has been postulated, the orientation of which increases steadily with increasing deformation before crystallization, until reaching a plateau due to relaxation, at deformation higher than the deformation at crystallization onset [25], [26] [27], [28], [29], [30], [31]. All these considerations agree on the key role played by the orientation of the amorphous chains on SIC.

The segmental orientation and SIC of crosslinked NR are strongly influenced by the crosslink density [17], [18], [25], [32], [33], [34]. Extensive studies performed on NR have shown that for sulfur-vulcanized NR the deformation marking the incipient crystallization of samples is nearly constant, regardless of crosslink density [17], [18], [25], [32], [33], but it decreases with an increase of crosslink density for peroxide crosslinked NR [34]. It is worth noting that the latter behavior is in agreement with the predictions of the classical rubber elasticity theory for homogeneous networks [14], [35]. Hence, a constant value of deformation at SIC onset has been interpreted as due to crosslink heterogeneity [17],

[18], [25], [32], [33], [34], [36], even though direct investigations have demonstrated that NR samples vulcanized by sulfur are characterized by a homogeneous distribution of crosslinks [37], [38].

The aim of this paper is the study of the effect of increasing crosslink density on the mechanical properties, the molecular chain orientation and SIC behavior of HNBR samples with an ACN content of 44 wt% and a residual unsaturation content of 9 %, vulcanized with various levels of sulfur curatives. The behavior of crosslinked samples is compared with that of the non-crosslinked counterpart. The study is carried out at room temperature, through ex-situ wide-angle X-ray fiber diffraction analysis, by gradually stretching virgin specimens that have not been subjected to any prior deformation. The elastomeric performances of rubbers, indeed, are critically dependent also on the possible occurrence of irreversible transformations taking place in as vulcanized samples in the first loading and successive unloading steps. This behavior measures the efficiency of an adopted vulcanization procedure and defines the elastomeric performances of rubbers in the loading/unloading cycles successive to the first one. The resultant information may be useful to compare SIC results on similar samples, subjected to different curing conditions.

Experimental Section

Materials. The sulfur-vulcanized HNBR samples have been supplied by Arlanxeo (Leverkusen, Germany). The starting HNBR Therban® 4498 VP has an ACN content of 44 wt%, a residual unsaturation content of 9 % and a Mooney viscosity ML 1+4 at 125 °C of 78 MU [8]. The density ρ of 0.98 g/cm^3 of the non-vulcanized HNBR sample was measured with an Elatest apparatus from Brabender GmbH & Co. KG (Germany). Stearic acid (Edenor C18-98 MY, ρ = 0.94 g/cm^3) was purchased by VWR International GmbH (Germany). Sulfur (S), zinc oxide (ZnO), mercaptobenzothiazole (MBT), and tetramethylthiuram disulfide (TMTD) (see Scheme 1) were purchased under the product names Rhenogran S-80 (ρ = 1.64 g/cm^3), Zinkoxid Aktiv (5,68 g/cm^3), Rhenogran MBT-80 (1.33 g/cm^3), and Rhenogran TMTD-70 (1.22 g/cm^3), respectively, from Lanxess AG (Germany). The densities of these ingredients were taken from the specifications of the manufacturer. Rhenogran S-80, Rhenogran MBT-80, and Rhenogran TMTD-70 are batched products with a S, MBT, and TMTD content of 80, 80, and 70 wt%, respectively.

The curative package includes sulfur as crosslinker, 1 phr of stearic acid (phr = part per hundred of rubber), 5 phr of zinc oxide, MBT and TMTD as primary and secondary accelerators, respectively (Table 1). For all HNBR samples, the contents of sulfur crosslinker and MBT and TMTD accelerators vary, while keeping the S/MBT and S/TMTD ratios constant at 2.98 and 1.50, respectively. This implies an increase in the crosslink density with increasing sulfur content from 0.38 to 3.01 phr, but similar network structures and lengths of sulfur crosslinks for all the vulcanized rubbers. The samples are coded as HNBR-NV for the non-vulcanized sample, and as HNBR-x, with x indicating the amount of sulfur in the compounds, for the vulcanized samples. Mixing was carried out on a two-roll mill from Troester GmbH & Co. KG with 20 cm roll diameter, 1.2 friction, 40 °C roll temperature, and at 20 rpm roll speed. The total milling time was kept at 10 min for all compounds. During this milling period the revolving rubber sheet was cut five times, and, finally, it was rolled and passed through the mill nip three times. A Monsanto MDR 2000E rheometer was used to determine the t_{90}-time at 160 °C according to DIN 53529. Square rubber slabs with 100 mm in width and length and with a thickness of 1.0 to 1.2 mm were vulcanized between polytetrafluoroethylene foils via compression molding for t_{90} plus 10 % at 160 °C and 120 bar. The quantities and compositions of the sulfur vulcanization systems and the bulk density ρ of the non-vulcanized and vulcanized HNBR samples are reported in Table 1. Note that the samples are so-called gum-stock samples without any filler or plasticizer.

Table 1. Composition, bulk density and crosslink density of the sulfur-vulcanized HNBR samples.[a,b]

Sample	Sulfur (phr)	MBT (phr)	TMTD (phr)	ρ Bulk Density[c] (g cm^{-3})	ν_e Crosslink density[d] (10^5 mol cm^{-3})	Weight loss[e] (%)
HNBR-NV	0	0	0	0.98	-	-
HNBR-0.38	0.38	0.13	0.25	1.022	4.8	7.1
HNBR-0.75	0.75	0.25	0.5	1.025	26	3.1
HNBR-1.1	1.13	0.38	0.75	1.027	35	2.9
HNBR-1.5	1.5	0.5	1	1.030	46	3.2
HNBR-1.9	1.88	0.63	1.25	1.032	56	4.0
HNBR-2.3	2.26	0.76	1.5	1.035	65	3.6
HNBR-3.0	3.01	1	2	1.039	75	4.5

[a)]The formulations of the rubber compounds are in part per hundred of rubber (phr). [b)]All samples contain 1 phr of stearic acid and 5 phr of ZnO. [c)]The values of bulk density ρ are calculated using the sample

compositions and the densities of the individual components, i.e. HNBR, S, stearic acid, ZnO, MBT, and TMTD. [d] The relative error is ≈5%. [e] Calculated as 100 (w_i-w_d)/w_i

Equilibrium swelling. The slabs of the vulcanized samples are cut in squared parts of approximately 2.5 mg (≈ 5 mm x 5 mm). The parts are weighed (initial weight w_{sw}) and then immersed in methyl ethyl ketone (MEK; Alpha Caesar, molar volume V_S = 90.2 cm^3 mol^{-1}; density ρ_S = 0.8054 g cm^{-3}) at *RT*. The solvent is renewed every 24 h. The swollen samples are removed from the solvent, gently blotted with an adsorbing paper to remove the excess of MEK at the surface and weighed every 10 to 12 h, until reaching a constant weight (w_{sw}) in approximately 72 h. Finally, the samples are dried in a vacuum oven at 72°C achieving a constant weight (w_d) in ~24 h. The volume fraction of the crosslinked rubbers at swelling equilibrium φ_r is calculated as:

$$\varphi_r = \frac{w_d/\rho}{w_d/\rho+(w_{sw}-w_d)/\rho_s} \qquad (1)$$

where (w_{sw} - w_d) corresponds to the quantity of absorbed solvent at equilibium.

The crosslink density, ν_e, is calculated as prescribed by the classical Flory-Rehner Equation, in the assumption that the functionality of the crosslinks is 4 and the crosslinked network is homogeneous [39]:

$$\nu_e = -\frac{ln(1-\varphi_r)+\varphi_r+\chi\varphi_r^2}{V_s\left(\varphi_r^{1/3}-\frac{\varphi_r}{2}\right)} \qquad (2)$$

In Equation 2, χ is the Flory-Huggins interaction parameter which, for the HNBR-MEK combination, is 0.453 [40], [41].

The values of the crosslink densities, averaged over the results of 5 independent measurements, are reported in Table 1, and presented in Fig. S1 as a function of the amount of sulfur added for vulcanization. The crosslink density increases with increasing sulfur content in a concave fashion. The amount of trapped entanglements may also vary and tends to zero as the density of chemical crosslinks tends to zero.

Differential scanning calorimetry (DSC). DSC scans are recorded with a differential scanning calorimeter (Mettler Toledo DSC-822) under a nitrogen atmosphere with a scanning rate of 10 °C/min in a temperature range from -70 to 100 °C. The values of the glass transition temperature (T_g) are determined from the second heating scans at the midpoints of the heat capacity jumps.

X-ray diffraction. Wide angle X-ray powder diffraction (WAXS) profiles are recorded at *RT* with an Empyrean diffractometer (Malvern Panalytical) in reflection geometry (θ-θ scans, with θ half of diffraction angle) using CuKα radiation (λ =1.5418 Å) at a scanning rate of 0.0705 deg (2θ)/s.

Two-dimensional WAXS fiber diffraction patterns were recorded with a Bruker-Nonius Kappa CCD diffractometer (MoKα radiation, λ = 0.71073 Å) on stretched specimens. Measurements were performed on rubber specimens that were gradually stretched at different strains, while keeping the samples in tension, using a custom-made tensile apparatus with an estimated average strain rate of 2 min^{-1}. Additional measurements were also performed on the non-crosslinked sample, by stretching independent specimens at various deformations with strain rate of 10 min^{-1}. For each imposed deformation value, 5 images of 1 min/image were collected and then added together. Radial, equatorial, meridional and azimuthal one-dimensional profiles were extracted from the two-dimensional WAXS patterns by using the freeware software Fit2D [42], as shown in Fig. S2. In particular, azimuthal profiles spanning a narrow 2θ range centred around the equatorial reflection at 2θ(MoKα) ≈ 8.4° (i.e. 7.4≤2θ ≤9.1°), corresponding to the interplanar distance *d* of ≈0.48 nm (Fig. S2D) and the meridional reflection at 2θ(MoKα) = 5.7° ((i.e. 4.7≤2θ ≤6.7°), corresponding to the interplanar distance *d* of ≈ 0.72 nm are extracted from the two-dimensional WAXS images. Additional azimuthal profiles spanning a wider 2θ region encompassing the whole amorphous halo (i.e. 6.8≤2θ ≤13.2°) (Fig. S2E) are also extracted.

For each deformation, the degrees of orientation of the crystalline and amorphous phases of the HNBR stretched specimens were estimated from the azimuthal profile (Fig. S3), after careful subtraction of air and background contributions (see SI).

For the amorphous contribution to the azimuthal intensity distribution, the fitting function $I_{am}(\cos\varphi)$, where φ is the azimuthal angle (corresponding to the angle with respect to the tensile direction) (Fig. S2C), can be approximated by a linear combination of even-order Legendre polynomials P_n, truncated to the 4th order [43], [44]. Equivalently, it can be approximated by Equation:

$$I_{am}(t) = A + B\cos^2\varphi + C\cos^4\varphi \qquad (3)$$

The crystalline contribution to the azimuthal intensity distribution $I_{cr}(t)$ is approximated by a Gaussian function centered at φ=90°:

$$I_{cr}(t) = \frac{G}{b[\pi/(4\ln 2)]^{0.5}} \exp\left[\frac{4\ln 2(\varphi-90)^2}{b^2}\right] \quad (4)$$

where G and b are the area and the width at mid-height of the Gaussian function.

The degree of orientation for the amorphous (x=am) and crystalline (x=cr) phases is measured by the average coefficients associated to the second and fourth Legendre polynomials $P_2^{WAXS\text{-}x}$ and $P_4^{WAXS\text{-}x}$ [43], [44] as given by Equations 5 and 5':

$$P_2^{WAXS-X} = \frac{1}{2}(3\langle\cos^2\varphi\rangle_x - 1) \quad (5)$$

$$P_4^{WAXS-X} = \frac{1}{8}(35\langle\cos^4\varphi\rangle_x - 30\langle\cos^2\varphi\rangle_x + 3) \quad (5')$$

where $\langle\cos^n\varphi\rangle_x$ is the mean square of $\cos^n\varphi$ (n=2,4) and it is calculated by Equation 6:

$$\langle\cos^n\varphi\rangle_x = \frac{\int_0^{\pi/2} I_x(\cos\varphi)\cos^n\varphi\sin\varphi d\varphi}{\int_0^{\pi/2} I_x(\cos\varphi)\sin\varphi d\varphi} \quad (6)$$

In Equation 6, I_x corresponds to the contribution to the WAXS intensity from the amorphous phase I_{am} (Equation 3) for the calculation of $\langle\cos^n\varphi\rangle_{am}$, from the crystalline phase I_{cr} for the calculation of $\langle\cos^n\varphi\rangle_{cr}$.

Equation 5 entails that the order parameter $P_2^{WAXS\text{-}x}$ is 1 for a perfect orientation of the correlation distance vectors in the direction parallel to the stretching direction, -0.5 for an orientation perpendicular to the stretching direction, and 0 for isotropic orientation, whereas the corresponding values for $P_4^{WAXS\text{-}x}$ are 1, 0.375 and 0, respectively. Since the polarization of the amorphous halo and the strongest reflection due to the crystallization of the alternating TMAC sequences occurs on the equator, there is a negative (not known quantitatively) factor between the values of the order parameter marking the orientation of the amorphous and crystalline segments and the order parameters measured from X ray patterns $P_2^{WAXS\text{-}x}$ [43], [44].

Based on Equations 3, 5, 5' and 6 the values of $P_2^{WAXS\text{-}am}$ and $P_4^{WAXS\text{-}am}$ were calculated as:

$$P_2^{WAXS-am} = \frac{14B+12C}{105A+35B+21C} \quad (7)$$

$$P_4^{WAXS-am} = \frac{8C}{315\,A+105B+63C} \qquad (7')$$

The fiber WAXS analysis, repeated for selected experiments, indicates that the values of the order parameters of the amorphous phase are affected by 10% relative error.

From the azimuthal profiles of the kind shown in Fig. S3C, an approximate index of crystallinity x_c was also evaluated from the relative intensity of the equatorial reflection at $2\theta(\text{MoK}\alpha)\approx 8.4°$ (equatorial crystallinity index), that is $x_c = 100 \times A_c / A_{tot}$, where A_c is the area of the crystalline peaks at $2\theta \approx 8.4°$ and A_{tot} is the area subtending the whole profile integrated over the narrow 2θ region comprised between 7.4 and 9.4°, as indicated in Fig. S3C''.

Mechanical tests. Mechanical tests were performed at *RT* by stretching dumbbell-shaped specimens, cut from the rubber slabs with a thickness of 1.0 to 1.2 mm, a width of 3 mm and a gauge length of 15 mm, using a universal testing machine (Instron 5566H1543), according to the Standard Test Method ASTM D638.

The drawing speed was set equal to 10 times the initial gauge length L_0 per min (150 mm/min) corresponding to a strain rate $v = 10\ \text{min}^{-1}$ (= $0.17\ \text{s}^{-1}$) for the measurement of the stress strain curves and the consequent determination of the tensile parameters up to breaking, and to $0.1 \times L_0$ per min (1.5 mm/min) corresponding to $v = 0.1\ \text{min}^{-1}$ (= $1.7 \times 10^{-3}\ \text{s}^{-1}$) for the measurement of the Young's moduli.

The tension set after break (t_b) was measured according to the Standard Test Method ASTM D412 on dumbbell-shaped specimens stretched up to breaking, that is up to a final deformation $\varepsilon_b = 100 \times (L_b – L_0) / L_0$, with L_b the final length achieved at the break and L_0 the initial gauge length. The two broken pieces were fit together so that they were in good contact over the full area of the break and after ten min the length of the fully relaxed specimen L_{rb} was measured. The tension set (in %) after break was then calculated as $t_b = 100 \times (L_{rb} – L_0) / L_0$. Benchmarks were used to determine elongation.

Mechanical hysteresis cycles were performed at *RT* on dumbbell-shaped specimens. The specimens were stretched up to a deformation ε_{max} equal to 70 to 90 % of the strain at break, at a constant rate of 30 mm/min (strain rate $v = 2\ \text{min}^{-1} = 0.033\ \text{s}^{-1}$), and then relaxed at same strain rate. Three consecutive cycles

of stretching and relaxing were recorded with a waiting time of 10 min between one cycle and the successive one. After each cycle, the values of the residual deformation (tension set, t_s) and of the percentage of dissipated energy (W_{diss}, hysteresis) were measured. The values of the tension sets after a given cycle i were measured as $t_s(i) = [(L_{ri} - L_{0(i-1)}) / L_{0(i-1)}] \times 100$, where the subscript "$i$" ($i$-1) refers to the i-th ((i-1)-th) hysteresis cycle and L_{0i} and L_{ri} are the initial and final lengths of the relaxed specimen measured 10 minutes after the end of the cycle, respectively.

The stress strain curves, the hysteresis cycles and the values of the mechanical parameters were averaged over at least five independent experiments.

Result and Discussion

Thermal and structural analysis

The WAXS profiles recorded at *RT* and the DSC heating scans recorded at 10 °C/min of the HNBR samples are reported in Fig. 1 and 2, respectively.

All the samples are amorphous at *RT*, as indicated by the presence of a broad halo centered at $2\theta(CuK\alpha) \approx 19°$. The crystalline peaks present in the diffraction profiles of the crosslinked samples are due to zinc oxide from the curatives package and/or fillers added as slip agents (talc and clinochlore) (Fig. 1).

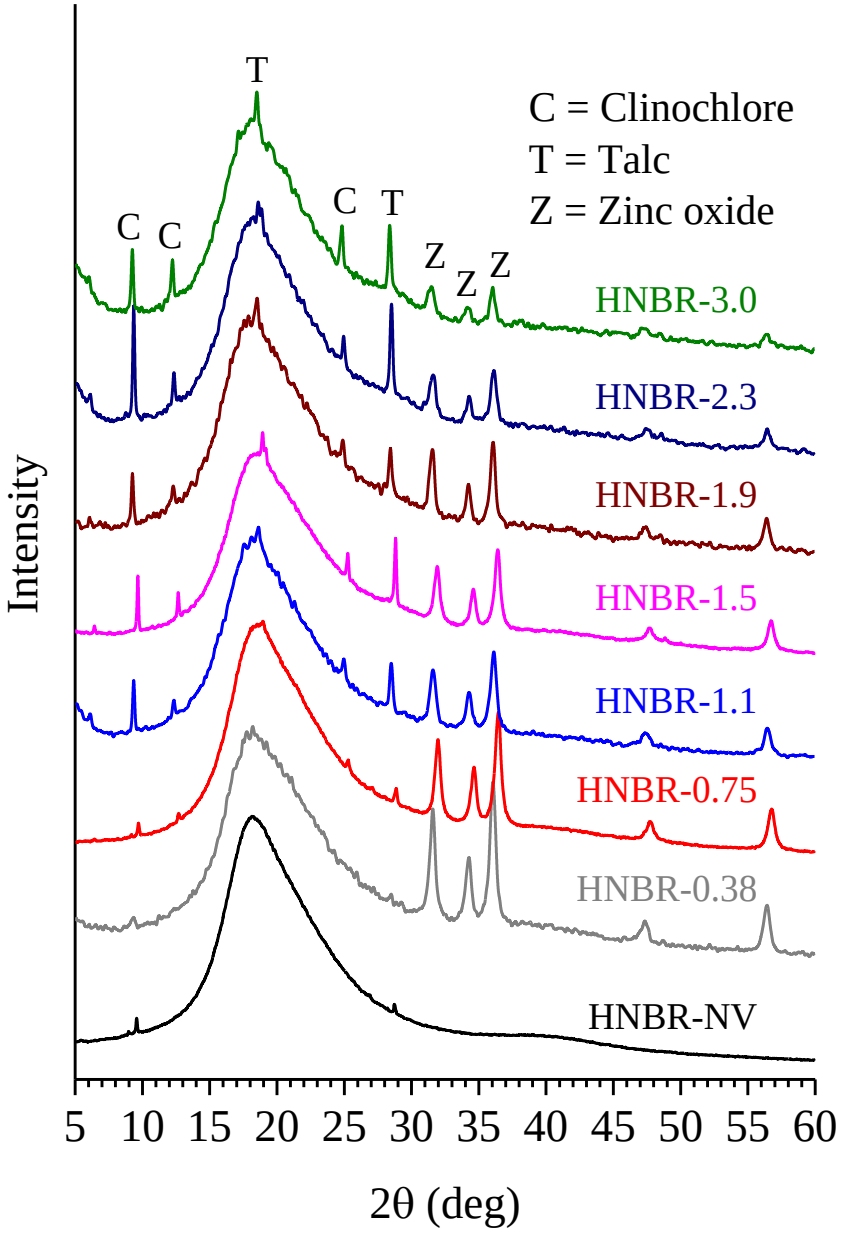

Fig. 1. X-ray powder diffraction profiles of non-vulcanized (NV) and vulcanized HNBR samples with varying sulfur curatives. The main reflections due to crystalline additives from curatives (Z, stands for ZnO) or from sample preparation (T and C stand for talc and clinochlore) are indicated.

The DSC thermograms of the HNBR samples (Fig. 2A) do not present any endothermic peak, but only an inflection point below *RT*, due to the glass transition, confirming that the samples are amorphous. The HNBR samples with 44 wt% of ACN do not experience thermally induced crystallization at low temperatures in the DSC thermograms of Fig. 2B, probably because of a slow kinetics. Thermally induced crystallization, indeed, has been evidenced for HNBR samples with ACN content of 34 and 36 wt% [45], [46], where crystallization emerges after suitable annealing at temperatures close to the glass transition, and it is due to the presence of long tetramethylene sequences forming polyethylene-like crystals. For the

HBNR samples with 44 wt% ACN crystallization of alternating TMAC sequence upon annealing at low temperatures may not be excluded.

The values of the glass transition temperature, T_g, determined from the DSC curves of Fig. 2A, are reported in Fig. 2B as a function of the crosslink density. An almost linear increase of the T_g values with increasing crosslink density is observed, due to the reduced mobility of the chains [47].

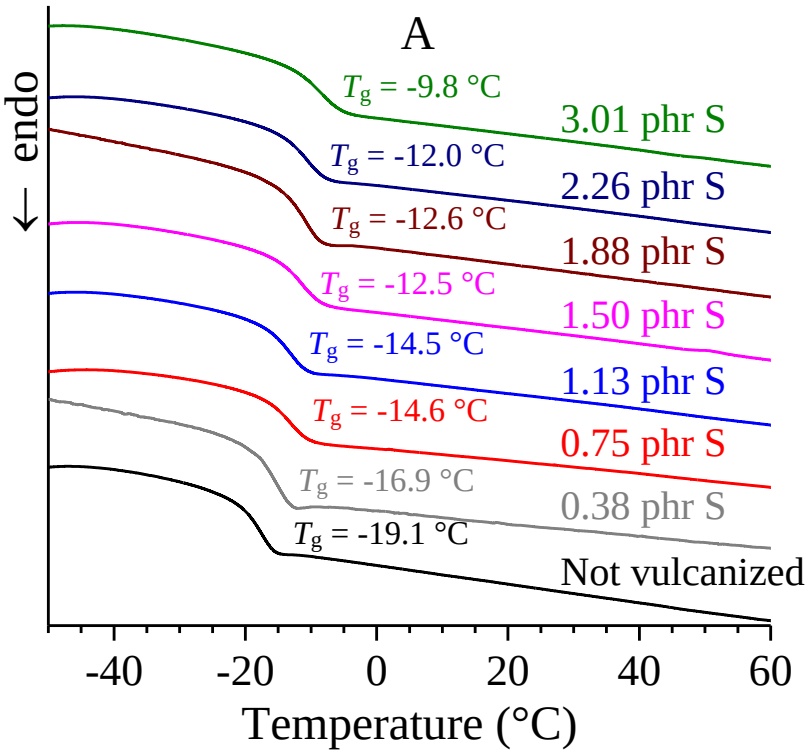

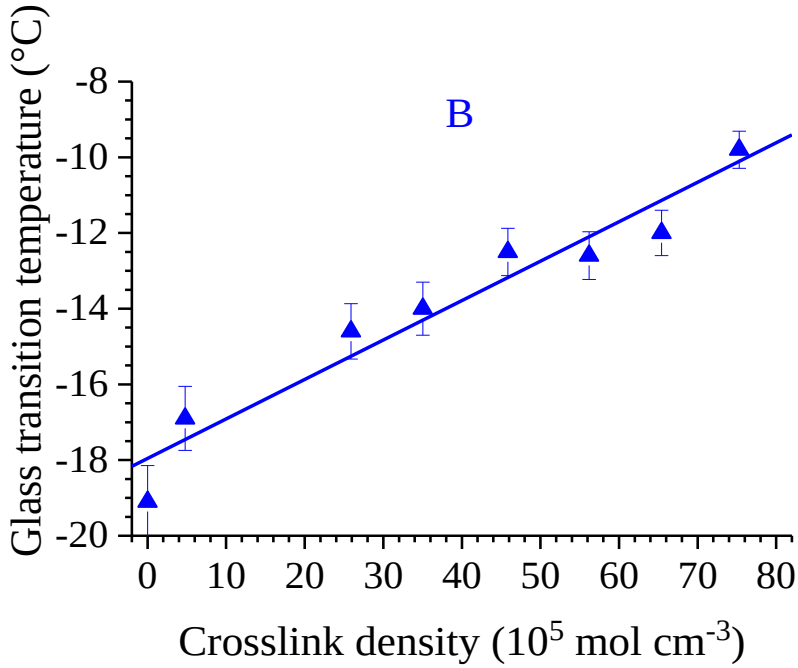

Fig. 2. A: DSC heating scans of HNBR samples with varying crosslink densities. Values of glass transition temperatures (T_g) are indicated. B: Corresponding plot of T_g-values as a function of crosslink density.

Mechanical properties

Stress-strain curves. The nominal stress-nominal strain curves recorded at *RT* of the non-vulcanized and vulcanized HNBR samples are shown in Fig. 3. The average values of the Young's modulus (E), elongation at break (ε_b), tensile strength at break (σ_b), and tension set at break (t_b) are reported in Table S1 and in Fig. 4 as a function of the crosslink density.

The stress-strain curves of the non-vulcanized sample, reported in Fig. 3A, shows a pronounced and broad yield followed by a stress drop due to the chain relaxation (strain softening), then a plateau region, in which the stress is almost constant with increasing the strain (cold drawing) and finally a steep increase of stress up to the breaking (strain-hardening). The sample shows high ductility with elongation at break of ≈1200% and good elastomeric properties with a value of tension set at break of only 18% (Fig. 3A and Table S1).

The vulcanized samples show stress-strain curves typical of hard rubbers with the stress that increases with strain, first rapidly up to about 20 – 30 % strain, then more slowly for higher strains from 20 – 30% to about 200 – 300 %, and finally again rapidly, up to the break, due to strain-hardening occurring at higher deformations (Fig. 3B). Moreover, with increasing crosslink density the values of stress at any strain increase, whereas the elongation at break tends to decrease (Fig. 3B and Table S1). Therefore, the increase of the crosslink density enhances the resistance to tensile deformation and induces a loss of ductility.

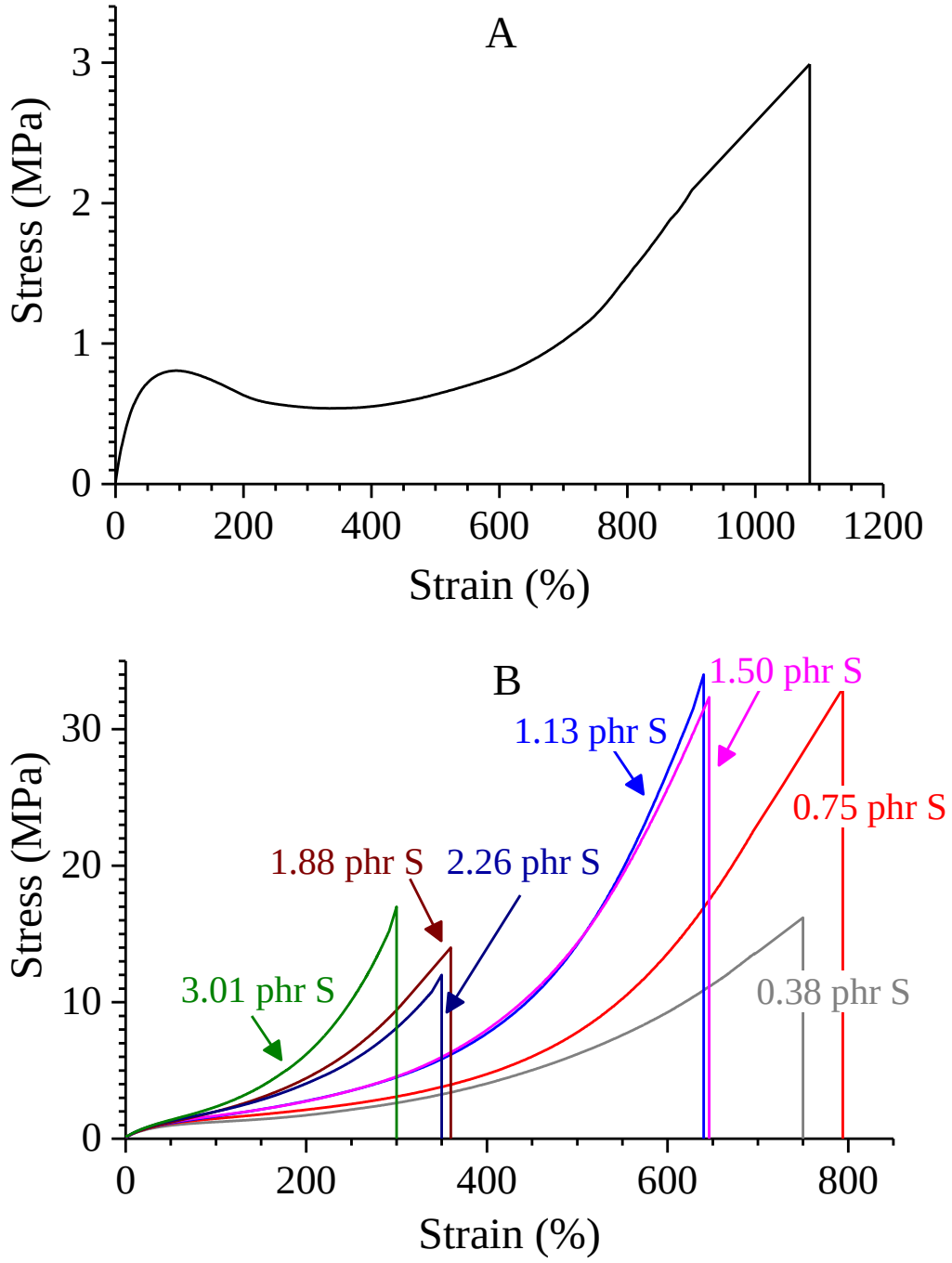

Fig. 3. Nominal stress-nominal strain curves of non-vulcanized (A) and vulcanized (B) HNBR samples with varying sulfur contents.

The vulcanized samples present values of the Young's modulus and stress at break significatively higher than those of the non-vulcanized rubber. In particular, the values of Young's modulus increases steeply from ≈1 MPa for the non-vulcanized sample to ≈3 MPa for the weakly crosslinked sample and tend to increase with increasing crosslink density less steeply (Fig. 4A). The stress at break first increases with increasing ν_e, reaches a maximum for samples with ν_e around 20-50 $\times$ 10^{-5} mol cm^{-3} and then decreases by a further increase of ν_e reaching a quasi-plateau (Fig. 4B). The deformation at break, instead, decreases with the increase of ν_e (Fig. 4C). Finally, all the samples, including the non-vulcanized one, have good elastomeric properties in the whole range of deformations up to the break, as indicated by the values of tension set at break that are lower than 64% (Fig. 4D and Table S1).

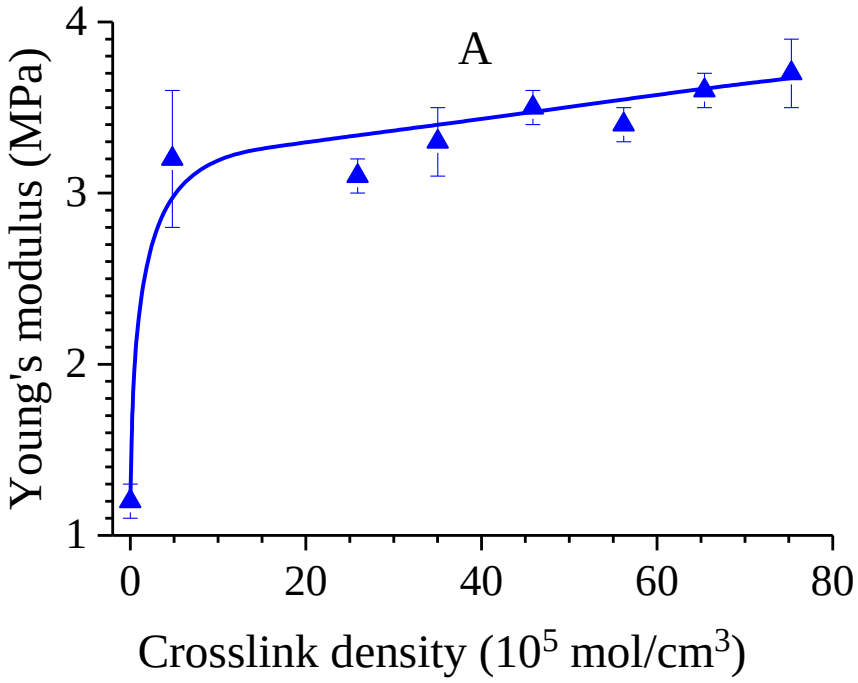
A
Young's modulus (MPa)
1
2
3
4
0
20
40
60
80
Crosslink density (10^5 mol/cm^3)

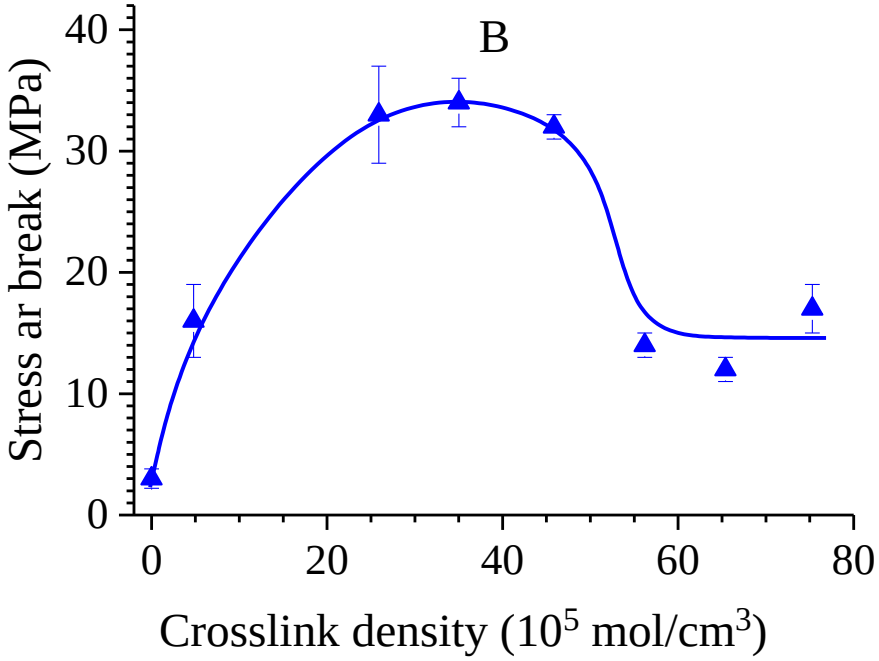
B
Stress ar break (MPa)
0
10
20
30
40
0
20
40
60
80
Crosslink density (10^5 mol/cm^3)

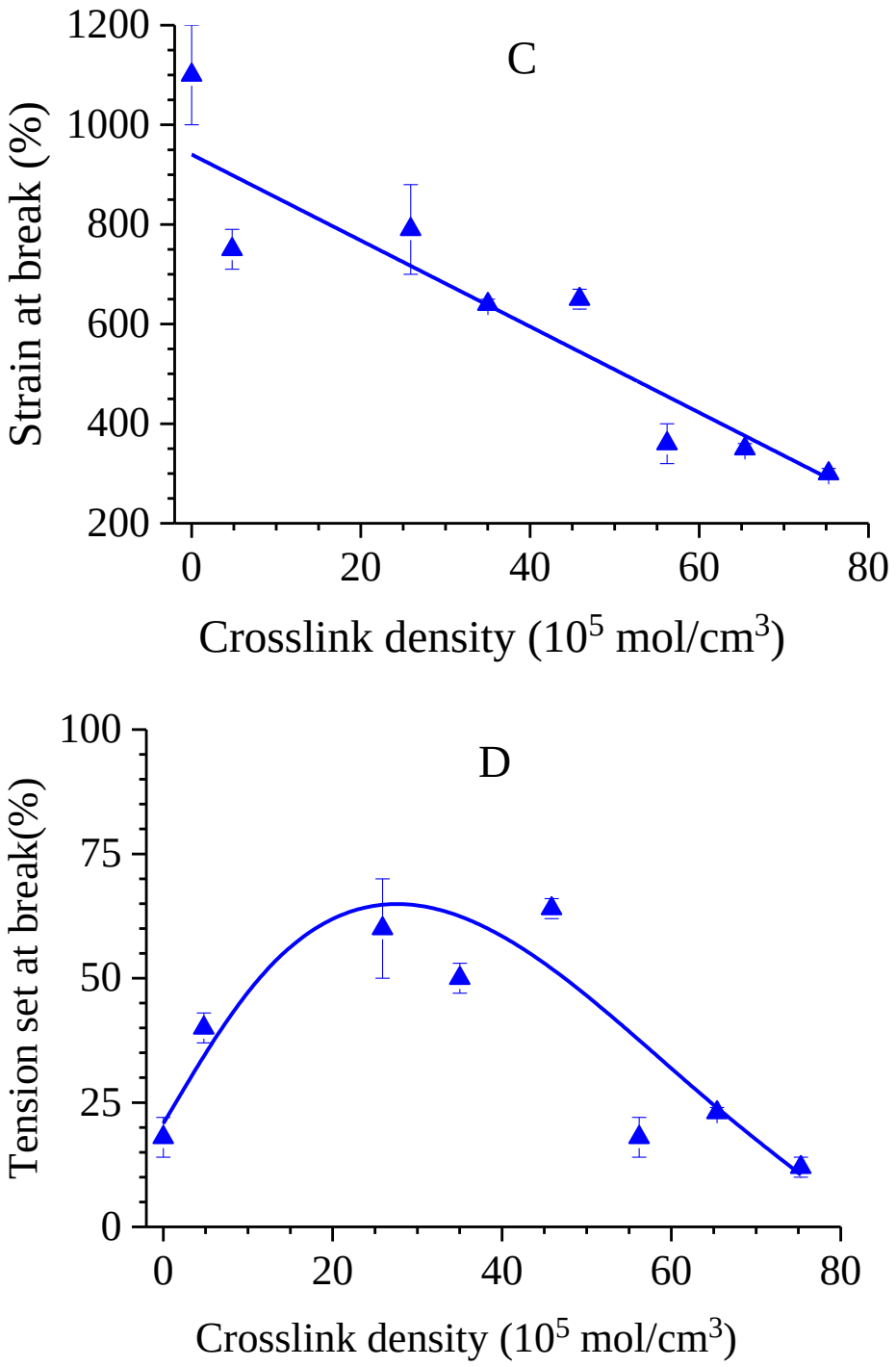

Fig. 4. Values of Young's modulus (A) and stress (B), strain (C) and tension set (D) at break as a function of crosslink density, for HNBRs samples with varying crosslink densities.

Hysteresis cycles. The hysteresis cycles of the HNBR samples with different crosslink densities are reported in Fig. 5 and S4. The values of the tension set and the percentage of dissipated energy (t_s and W_{diss}) measured after the first and the successive cycles are listed in Table S2. Since the maximum deformation achieved during the cycles (ε_{max}) is different for the various HNBR samples, in order to

compare the elastomeric performances of the different samples, the values of tension set after each cycle are divided by ε_{max}, obtaining the percentages of residual deformation after the release of the tensile force (percentages of permanent set). These values and the percentage of dissipated energy across the different hysteresis cycles are reported in Fig. 6 as a function of the crosslink density.

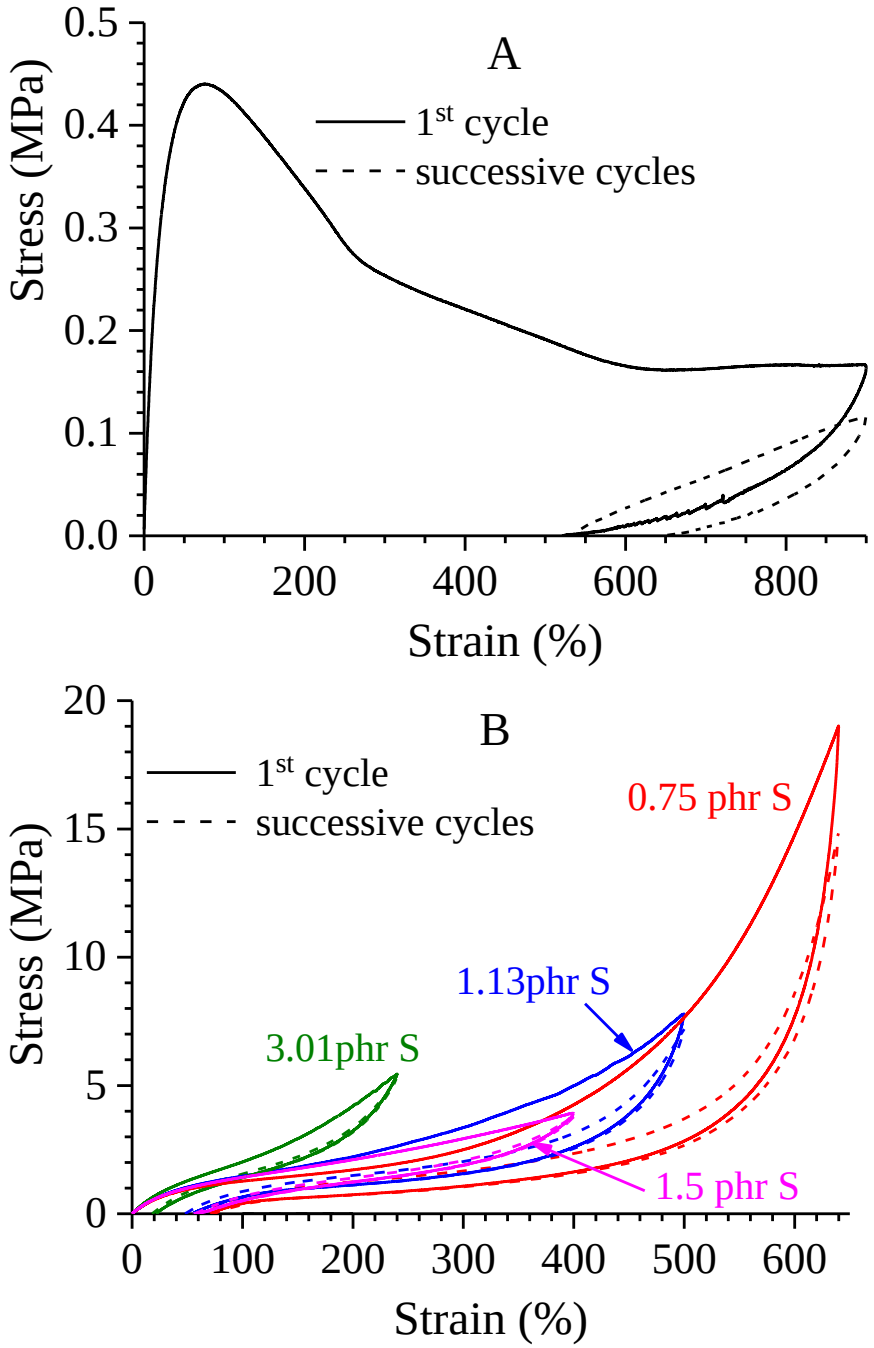

Fig. 5. Hysteresis cycles of non-vulcanized (A) and vulcanized (B) HNBR samples with different crosslink densities.

The non-crosslinked sample shows pronounced hysteresis, with a percentage of dissipated energy greater than 90% and large values of residual deformation after all cycles (Fig. 5A and Table S2). In fact,

due to the absence of chemical crosslinks between the chains, disentanglement and irreversible segmental relaxation phenomena occur during stretching, so that, upon retraction, the rubber does not regain its original length because the elastic energy is largely dissipated.

Conversely, vulcanized rubbers show good elastomeric properties when subjected to consecutive mechanical cycles of stretching and relaxing. The specimens do not fully recover their original length after the first cycle, and part of the energy expended during deformation is dissipated, as indicated by the percentages of residual deformation (t_s/ε_{max}) of about 10-15 % and hysteresis of about 30 – 55 % measured after the first cycle (Fig. 6A,B and Table S2). In the successive two cycles, however, the percentages of permanent set reduce to almost zero (Table S2) and the percentages of energy loss decrease by at least 50 % compared with the values relative to the first cycle (Fig. 6 and Table S2), indicating excellent elastomeric properties with little hysteresis.

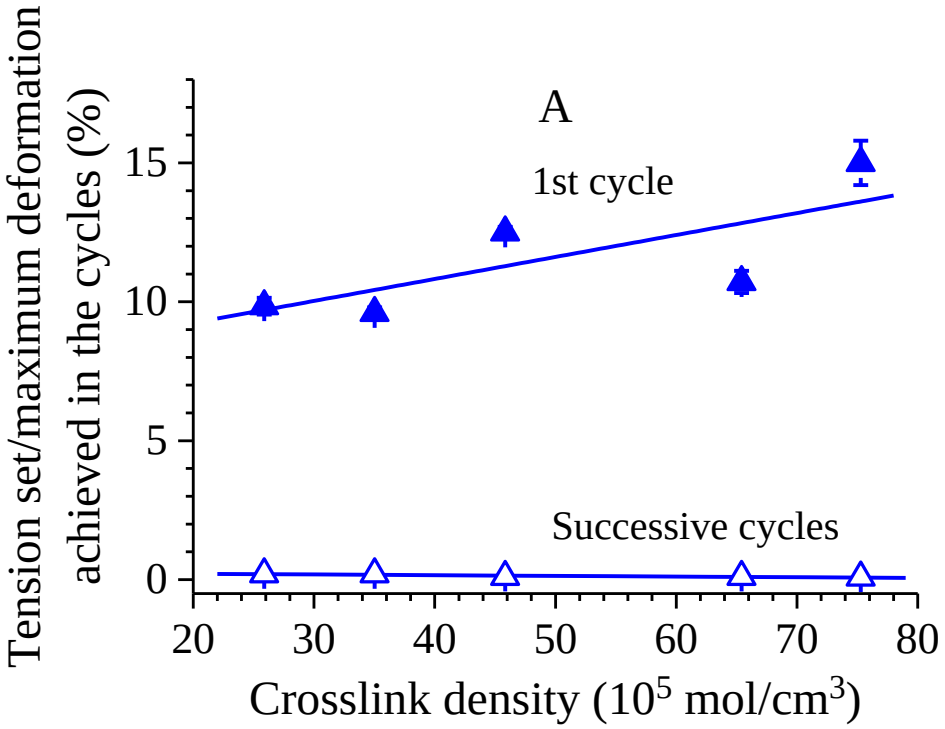

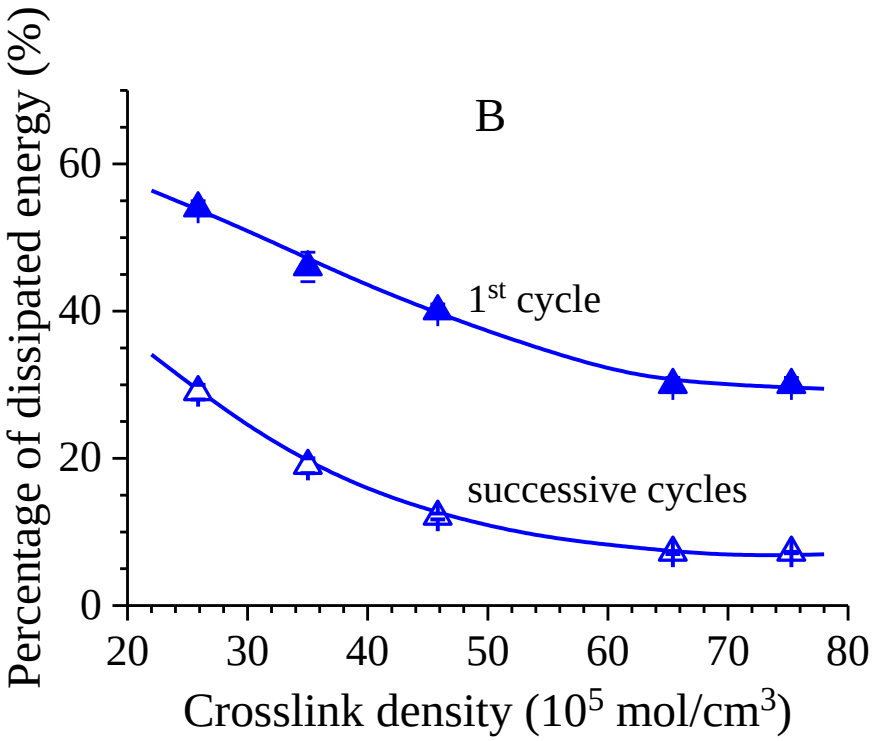

Fig. 6. Percentage of permanent set (t_s/ε_{max}, A) and of dissipated energy (B) after first (solid symbols) and successive hysteresis cycles (open symbols) of vulcanized HNBR samples with varying crosslink densities.

It is worth noting that for all samples the values of tension set measured in the first hysteresis cycle, after a deformation $\varepsilon_{max} < \varepsilon_b$, are always greater than those measured after the break, t_b (Tables S1 and S2). This is probably due to the slower strain rate at which the hysteresis cycles are performed (0.033 s^{-1}) with respect to that employed in the stress-strain tests (0.17 s^{-1}). This indicates that a characteristic relaxation time of the initial material should be within the time window defined by the inverse rates of the tensile tests and hysteresis cycles. As a result, after the first hysteresis cycle, the samples are subjected to a plastic (irreversible) deformation greater than that achieved after the break, upon the abrupt release of the tension. As this relaxation effect is limited to the first cycle, it may correspond to some degree of chain reorganization at the scale the crosslinking network, rather than to the intrinsic viscoelasticity of the material, that is to local frictional forces caused by the high local viscosity.

This effect is dramatically enhanced in the non-crosslinked sample (tension set measured in first hysteresis cycle 530% vs 18% after break), indicating considerable relaxation (viscous flow) within the

corresponding time window. In contrast to the vulcanized samples, this behavior may be related to the viscoelastic response of the non-vulcanized sample, which does not exhibit a true rubbery plateau.

Fiber diffraction analysis and strain-induced crystallization

The two-dimensional WAXS fiber patterns collected at *RT* of selected HNBR samples with different crosslink densities are reported in Fig. 7, S5 and S6. The analysis is carried out on specimens that have not been subjected to any prior deformation. For each sample, the two-dimensional WAXS patterns were recorded for the undeformed sample ($\varepsilon = 0$) and for samples stretched at different strains ε up to a deformation ε_{max} close to the break and then after the successive retraction paths from ε_{max} down to complete release of the tension (Force = 0).

The one-dimensional equatorial, meridional, azimuthal and radial profiles, obtained from the two-dimensional patterns of all HNBRs recorded at the different strains are reported in Fig. S7-S11.

For all samples, the two-dimensional WAXS patterns of the unstretched specimens (at $\varepsilon = 0$) show a halo centered at $2\theta(\text{MoK}\alpha) \approx 8.7°$ (i.e., $2\theta(\text{CuK}\alpha) = 19.2°$), the intensity of which is uniformly distributed along the whole azimuthal arc (Fig. 7, S7 – S11). This indicates that the samples are initially amorphous and that the amorphous phase is not oriented.

The two-dimensional patterns of the vulcanized samples (Fig. 7) show Debye-Scherrer rings due to the crystalline additives, regardless of deformation (see also Fig. 1). The intensity distribution of the amorphous halo tends to become anisotropic with increasing deformation, (Fig. 7), as indicated by the increase of intensity on the equator (at $\varphi=90$) in the azimuthal profiles of Fig. S8. The 2θ position of the amorphous halo, instead, regardless of the crosslink density, remains almost constant at $\approx 8.7°(\text{MoK}\alpha)$, as evident from the corresponding equatorial and radial profiles of Fig. S10 and S11, respectively. This indicates that the chain segments of the amorphous phase gradually align along the stretching direction with increase of deformation while keeping a short range correlation transversal to the stretching direction at distance of about $(2 \sin \theta/\lambda)^{-1} \approx 0.47$ nm as in the undeformed state.

Upon release of the tension the orientation is gradually lost, and the intensity of the amorphous halo appears again uniformly distributed along the entire azimuthal arc (Fig. 7, S7,S8).

It is worth noting that for the non-vulcanized sample HNBR-NV, the gradual stretching procedure adopted for the vulcanized counterparts (step-wise stretching at average strain rate of 2 min^{-1}) does not induce any significant change, as indicated by the uniform distribution of intensity of the amorphous halo centered at $2\theta(MoK\alpha) \approx 8.7°$, regardless of deformation (Fig. 7A-D and S7B-B'''). This indicates that in the adopted stretching conditions, in absence of crosslinks, the entanglements are not efficient enough to prevent the viscous flow of the chains. As a consequence, the elastomeric network is not deformed, because relaxation phenomena occur at the same or shorter time scales as the average deformation rate. This is fully coherent with the mechanical behavior of the non-vulcanized sample discussed above.

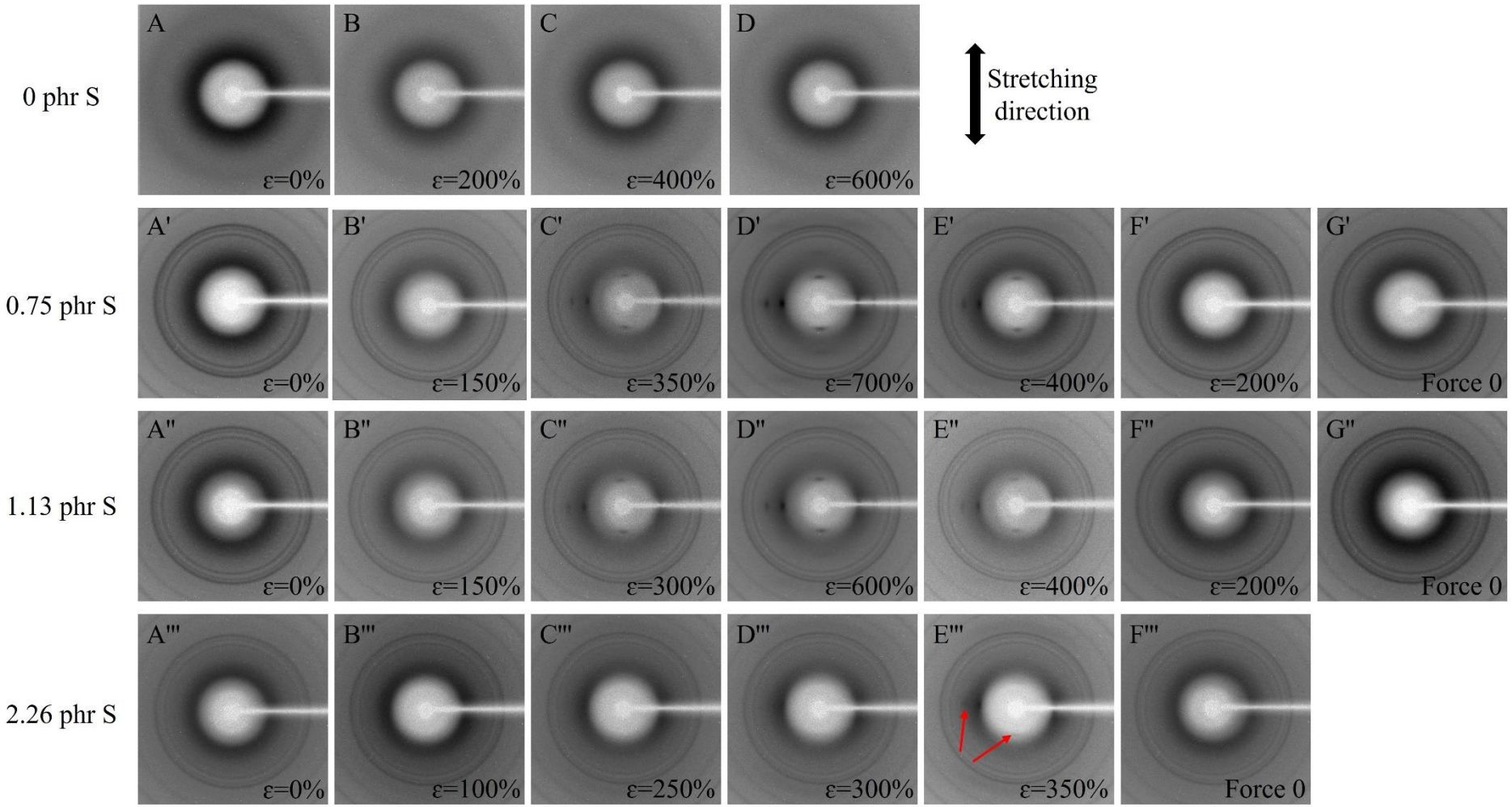

Fig. 7. Two-dimensional WAXS fiber patterns of non-vulcanized (A-D) and vulcanized samples (A'-G'; A''-G''; A'''-F''') with different crosslink densities, recorded at *RT* at the indicated deformations ε. Specimens that have not been subjected to any prior deformation are gradually stretched until reaching a deformation close to breaking, and then they are gradually relaxed until reaching complete relaxation (force zero, average deformation rate 2 min^{-1}). Arrows in E''' indicate reflections of faint intensity due to oriented crystallization of alternating TMAC sequences also for the highly crosslinked sample with 2.26 phr of sulfur. Stretching direction is indicated.

The vulcanized HNBR samples characterized by different crosslink densities show not only orientation of the amorphous phase but also SIC. For these samples, indeed, whereas at low strains (ε = 100 – 200 %) the sole observed changes are relative to the orientation of the amorphous phase, at strain greater than a critical value (250 – 300 %), well arched diffraction peaks appear on the equator at 2θ(MoKα) = 8.4 and 11.9° (interplanar distances $d \approx 0.48$ and 0.35 nm, respectively) and on the meridian 2θ(MoKα) = 5.7° ($d \approx 0.72$ nm) (Fig. 7, S5, S8-S11) due to the crystallization of the alternating TMAC sequences [9], [10], [11]. The chain axis periodicity evaluated from the meridional reflection at 2θ(MoKα) = 5.7° is close to a chain periodicity c = 7.2Å, consistent with a *trans*-planar conformation of the chains [9], [10], [11]. Upon release of the tension, the loss of orientation of the amorphous phase is preceded by the melting of the crystals, as indicated by the disappearance of the crystalline reflections (Fig. 7, S5, S8-S11) at deformation around 100-200%. Similar to NR the deformation at incipient crystallization during stretching is higher than the deformation marking the melting of crystals during the release of the tension [14], [25], [26], [27], [28].

The strain-induced crystallization and melting in consecutive cycles of stretching and release of the tension are mainly evident for the samples with crosslink density lower than 65 10^{-5} mol cm^{-3} (added sulfur content lower than 2.26 phr). Indeed, as the crosslink density increases, the crystalline reflections become broader and of low intensity, indicating that the correlation length of the crystals in the directions parallel and perpendicular to the chain axes decreases (Fig. S10). Furthermore, the deformation at incipient crystallization tends to increase with increasing crosslink density (Fig. S10). For instance, for the samples with the lowest crosslink densities HNBR-0.38 and HNBR-0.75 with ν_e equal to 4.8 and 26 10^{-5} mol cm^{-3}, respectively (added sulfur contents 0.38 and 0.75 phr, respectively, Fig. S10A,B,A',B') the crystallization onset is in between 250 and 300% whereas for the samples with the highest crosslink densities HNBR-2.3 and HNBR-3.0 with ν_e equal to 65 and 75 10^{-5} mol cm^{-3}, respectively (added sulfur contents 2.26 and 3.01 phr, respectively, Fig. S10F,G,F',G') the crystallization onset shifts to deformations higher than 300%, close to the elongation at break (300-400% Table S1).

The differences in SIC behavior of the vulcanized samples can be explained by assuming that a high crosslink density reduces the chain mobility, hindering the crystals lateral growth and somehow delaying the crystallization kinetics through a shift of the deformation marking the crystallization onset toward higher values (kinetic effect). Note also that the small increase of deformation at incipient crystallization with increasing the crosslink density is in contrast with the prediction on homogeneous networks by Flory [14], [28], and similar to the behavior of sulfur vulcanized NR [17], [18], [25], [32], [33], [48], [49]. How this discrepancy relates to possible crosslink heterogeneity (heterogeneity effect) and/or, as suggested by Fig. 5 and S4, to the occurrence of irreversible transformations during the first hysteresis cycle, remains uncertain at this point. According to ref. [48], indeed, for NR the inhomogeneity of the stretched network should play a key role as the corresponding SIC behavior is related to the stretching state of the network strands of shortest length [49]. Since the population of network strands is expected to increase with increase of crosslink density, the SIC behavior of the HNBR samples as a function of crosslink density suggests that the disturbance effect of the chemical crosslinks for the crystallization of the TMAC sequences prevails, determining a kinetic control of the SIC behavior.

For the non-vulcanized sample HNBR-NV, the gradual stretching in conditions similar to those adopted for the vulcanized samples (i.e. with an average strain rate of 2 min^{-1}) does not induce the orientation of the amorphous phase, probably because the loading time due to the application of the tensile force along with the time needed for stress transmission are longer than the characteristic segmental relaxation times. Also, no SIC occurs (Fig. 7A-D and S6B-B’’’). On the other hand, when independent HNBR-NV test specimens are stretched at a higher rate of 10 min^{-1}, the sample shows not only the orientation of the amorphous phase, but also SIC at deformations higher than some threshold (see Fig. S6 and S7A-A’’’), probably because the so-formed crystals prevent the viscous flow of the chains, since they act as physical knots of the elastomeric network. Therefore, these results support the hypothesis that whenever stretching does not induce any orientation of the amorphous phase, no SIC occurs.

The deformation-rate dependence of the structural behavior of the non-vulcanized sample HNB-NV, explains well the differences in mechanical behavior observed in the stress-strain curve recorded at strain

rate of 10 min^{-1} and in the hysteresis cycles recorded at strain rate of 2 min^{-1}. In fact, when the sample is stretched at high deformation rate, SIC occurs (Fig. S6) and it is responsible for the rapid upturn of the stress and the remarkable strain-hardening in the stress-strain curve recorded up to rupture (Fig. 3A). When the sample is instead stretched at low strain rate, SIC does not occur (Fig. 7A-D), and the sample undergoes viscous flow, resulting in large values of tension set and dissipated energy measured in successive stretching and relaxing cycles (Fig. 5A and Table S2).

For the vulcanized samples undergoing significant SIC (that is with added sulfur contents comprised between 0.38 to 2.26 phr), an index of crystallinity x_c was calculated from WAXS data, using the intensity of the equatorial reflection at $2\theta(MoK\alpha) \approx 8.4°$ as detailed in Fig. S3 (equatorial crystallinity index). The analysis was not carried out on the highly crosslinked sample with sulfur content equal to 3.01 phr, because of the too high uncertainty in the evaluation of x_c. The so-calculated values of x_c are reported in Fig. 8A, A' as a function of deformation.

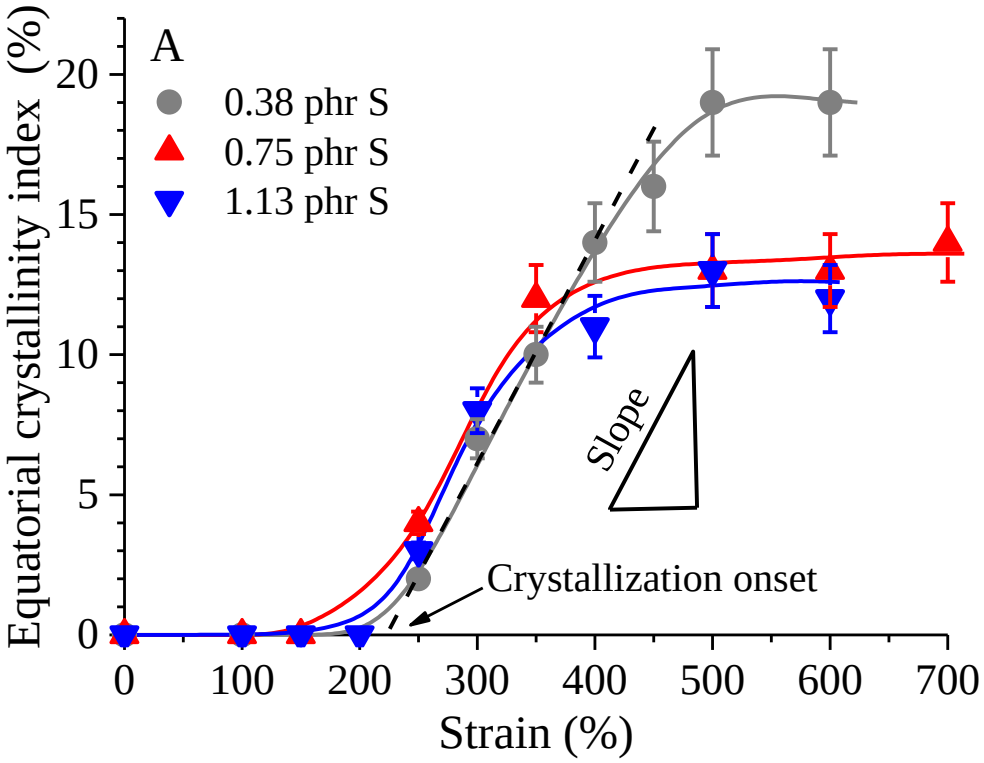
A
0.38 phr S
0.75 phr S
1.13 phr S
Slope
Crystallization onset
Equatorial crystallinity index (%)
Strain (%)
0
5
10
15
20
0
100
200
300
400
500
600
700

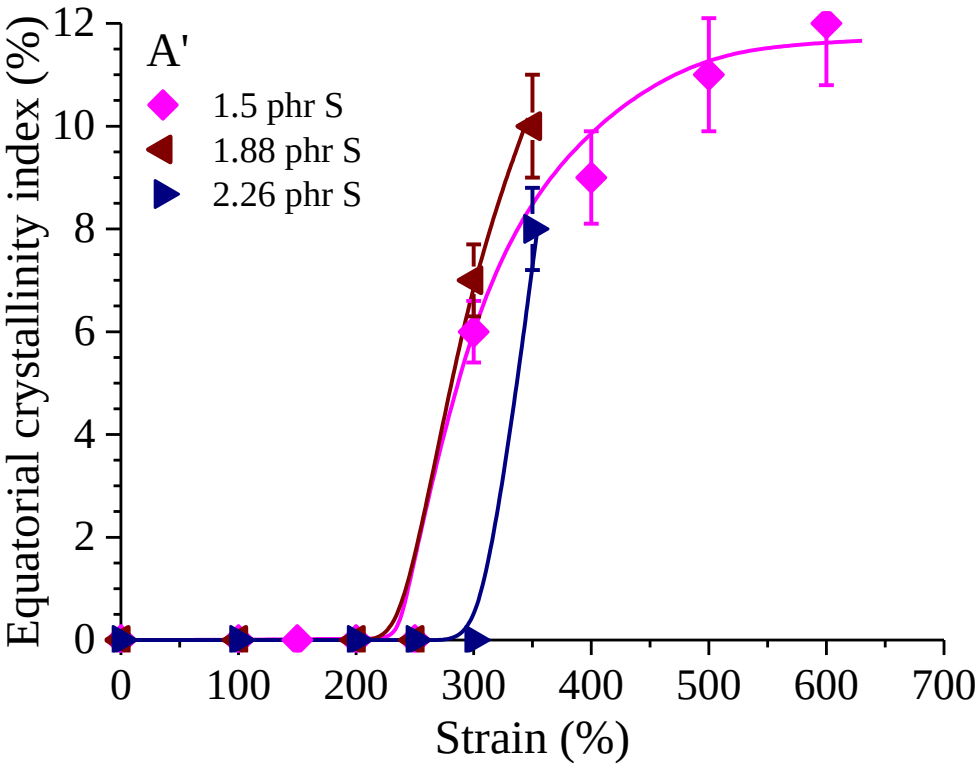
A'
1.5 phr S
1.88 phr S
2.26 phr S
Equatorial crystallinity index (%)
Strain (%)
0
2
4
6
8
10
12
0
100
200
300
400
500
600
700

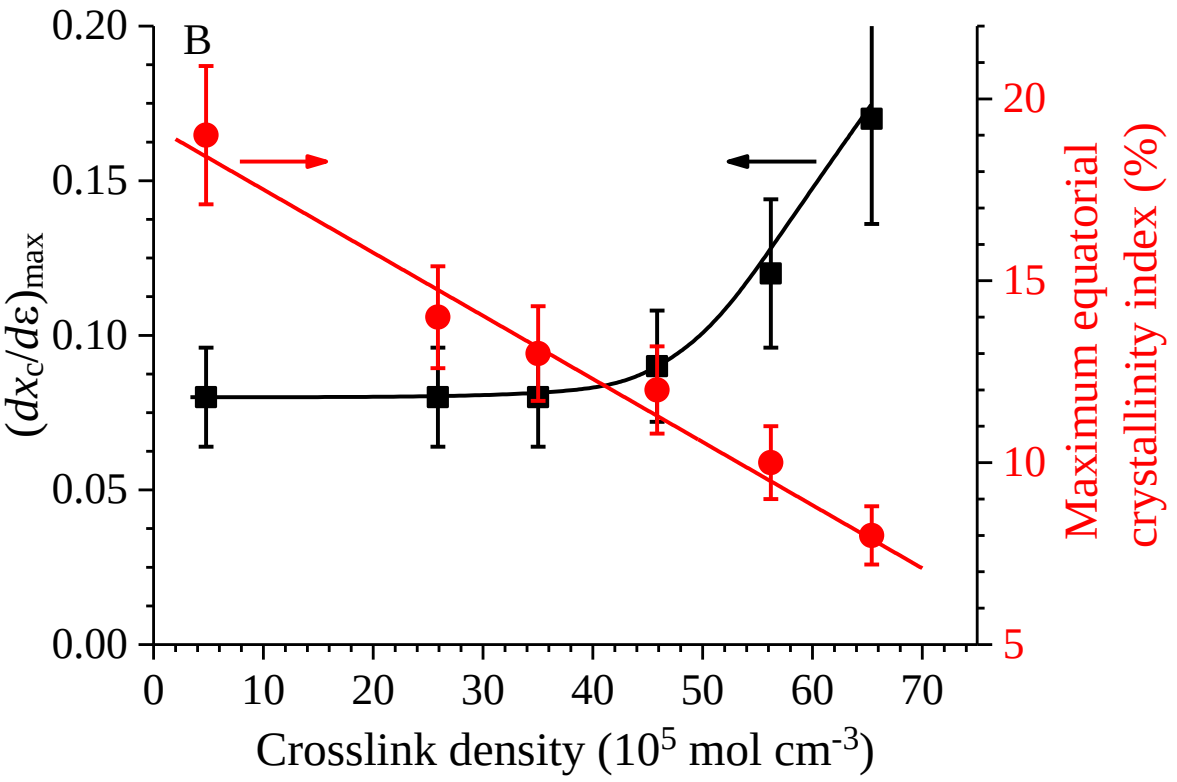

Fig. 8. Index of crystallinity x_c evaluated from WAXS data using the relative intensity ratio of the equatorial reflection at 2θ(MoKα)≈ 8.4 ° (equatorial crystallinity index) as detailed in Fig. S3C,C', as a function of the deformation (A, A') and values of the maximum increase of crystallinity index with increase of deformation $(dx_c/d\varepsilon)_{max}$ (left scale) and of the equatorial crystallinity index x_c(max) (right scale) achieved at the maximum deformation, close to rupture (Table 2), as a function of the crosslink density (B) for the HNBR samples experiencing significant SIC. The dashed line in A is the fit to the data with a straight line in the steepest region of the sigma-shaped curve. The intercept with the *x*-axis and the slope of the straight line are assumed to correspond to the deformation of incipient crystallization and to the maximum increase of the equatorial crystallinity index with respect to the deformation $(dx_c/d\varepsilon)_{max}$, respectively (A).

For all the samples, the equatorial crystallinity index increases with the increase of the deformation according to a sigmoidal curve, until reaching a maximum value at the highest approached strain, either because a plateau is approached, or because the sample ruptures (Table S1 and Fig. 8A,A'). The maximum value of the equatorial crystallinity index x_c(max) achieved upon stretching before the rupture of the sample decreases almost linearly with increasing the crosslink density (Fig. 8B, right scale). This decrease is due to the fact that with increasing the crosslink density, the length of the network strands decreases and also the length of crystallizable sequences decreases. Extrapolating the straight line of Fig. 8B to null crystallinity index allows to deduce that crystallization would not occur anymore for crosslink densities higher than ≈80 10^{-5} mol cm^{-3}. This suggests that the chemical crosslinks act as a sort of constitutional

defects of the rubber networks that not only shorten the length of crystallizable sequences, but also introduce topological constrains that reduce the segmental mobility and cause a decrease of ductility too (Fig. 4C).

The fit to the data with a straight line in the most-steep region of the sigmoidal curves is shown in Fig. 8A, as an example. The intercept with the *x*-axis and the slope of the straight line are assumed to correspond to an approximate value of the deformation at incipient crystallization and of incremental crystallinity index with respect to the deformation $(dx_c/d\varepsilon)_{max}$, respectively. Data of Fig. 8A, A' confirm that the values of deformation at incipient crystallization of specimens that have not been subjected to any previous deformation, although affected by a large relative error of ≈20%, are about constant and equal to 200% – 240 % for samples with crosslink densities below or equal to 56 10^{-5} mol cm^{-3} (added sulfur content ≤ 1.9 phr) and tend to increase to ≈300% for samples with crosslink densities above this threshold.

The values $(dx_c/d\varepsilon)_{max}$ are reported in Fig. 8B as a function of the crosslink density (left scale). Since the test specimens are stretched at similar strain rate (2 min^{-1}) and the WAXS profiles are recorded while keeping the samples in tension at each deformation for about 15 min, the incremental crystallinity index with respect to the deformation (the slope of the curves in the steepest part) may be considered to be a sort of a kinetic parameter of SIC ("SIC rate"), marking how fast the crystallinity increases by effect of stretching. Inspection of Fig. 8B indicates that the value of $(dx_c/d\varepsilon)_{max}$ is nearly constant at low crosslink density (*i.e.* for $\nu_e \leq 46\ 10^{-5}$ mol cm^{-3}, added sulfur content ≤1.50 phr), and increases for $\nu_e > 46\ 10^{-5}$ mol cm^{-3} (added sulfur content ≈1.5 phr).

It is worth noting that the increase of "SIC rate" with increasing crosslink density, as well as the associated decrease of crystal size and crystallinity index observed for the HNBR samples, are similar to the SIC behavior of natural rubber. For NR, indeed, it has been shown that a higher crosslink density results in a faster crystallization [13], [16], [23]. This increase has been ascribed to the increase of the nucleation density, as nucleation is controlled by the local stretch ratio of the network strands, which for highly crosslinked networks should be enhanced. The increase of the nucleation density with the increase

of the crosslink density, in turn, also causes the formation of crystallites of smaller size due to the restricted segmental mobility that hinders the lateral growth of the crystals [13], [16], [23]. As a result of the reduced mobility, also a decrease of the final degree of crystallinity occurs [13], [30, [31].

Segmental orientation

The segmental orientation of the HNBR samples stretched at different deformations is calculated from the azimuthal profiles extracted from the two-dimensional WAXS patterns using equations (7) and (7'), as detailed in Fig. S3 and in the Experimental Section.

For the standard statistics of polymer chains in the Gaussian approximation, the order parameter $P_2^{\text{WAXS-am}}$ of the amorphous segments depends on the elongation ratio $\lambda = L/L_0$ (=ε/100-1) through equation [38], [50]:

$$P_2^{WAXS-am} = K\nu_e(\lambda^2 - 1/\lambda) \qquad (8)$$

where K (in cm^3/mol), a negative quantity corresponding to a fraction of the monomer molar volume, accounts for the local structure of the amorphous phase [43], [44].

The values of the order parameters $P_2^{\text{WAXS-am}}$ and $P_2^{\text{WAXS-cr}}$ (Equation 4) for the amorphous and crystalline phases of the HNBR samples are reported in Fig. 9, as a function of the elongation parameter (λ^2-1/λ).

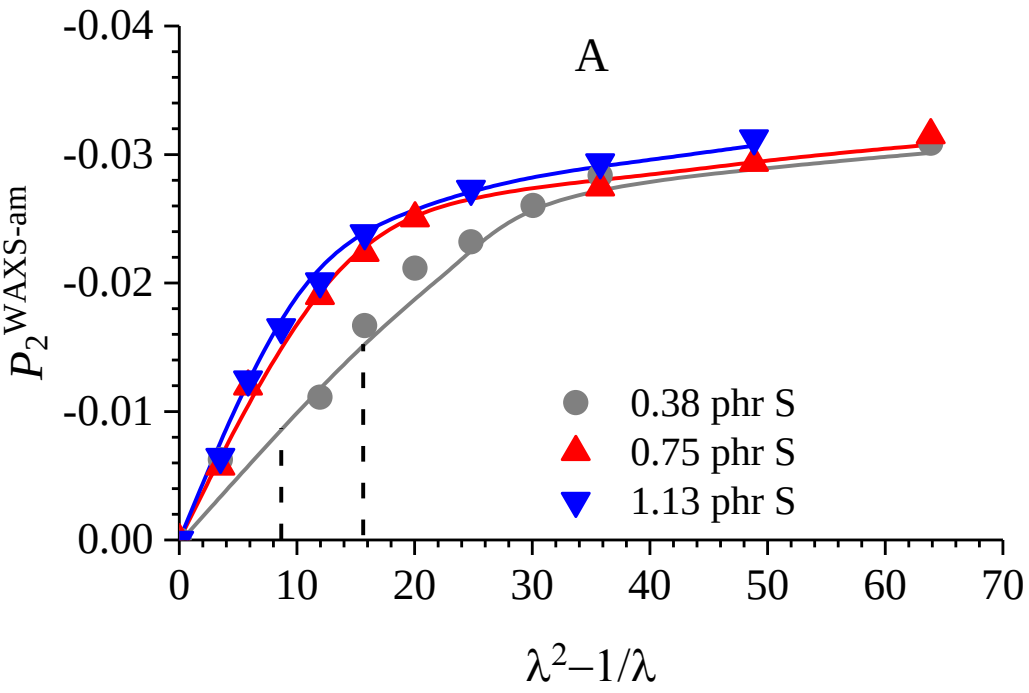
A
-0.04
-0.03
-0.02
-0.01
0.00
P_2WAXS-am
0
10
20
30
40
50
60
70
λ^2-1/λ
0.38 phr S
0.75 phr S
1.13 phr S

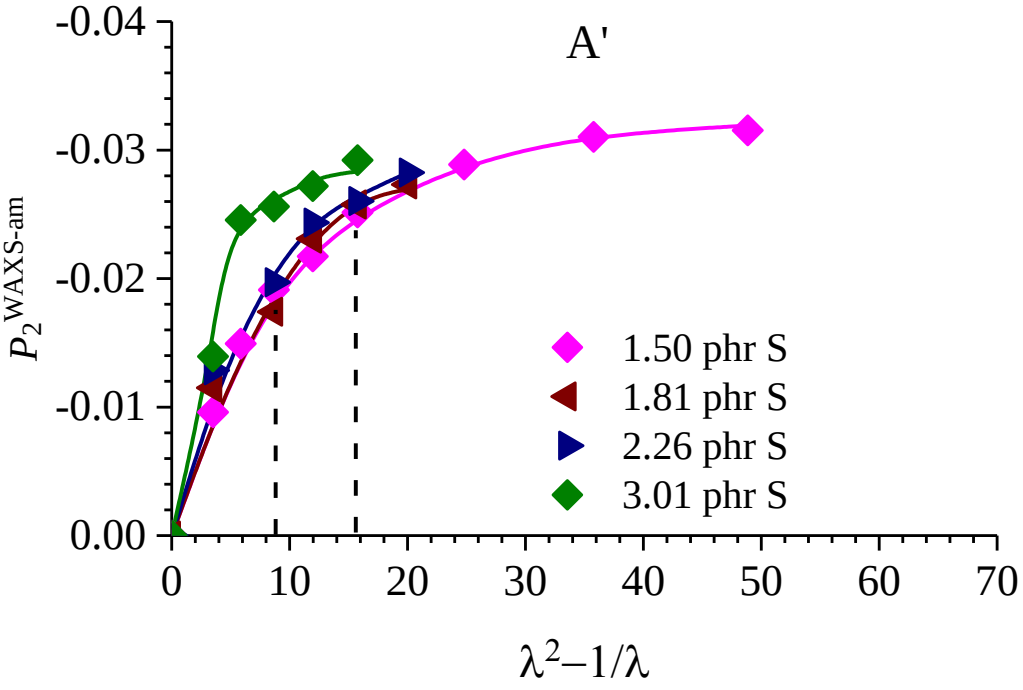
A'
-0.04
-0.03
-0.02
-0.01
0.00
P_2WAXS-am
0
10
20
30
40
50
60
70
λ^2-1/λ
1.50 phr S
1.81 phr S
2.26 phr S
3.01 phr S

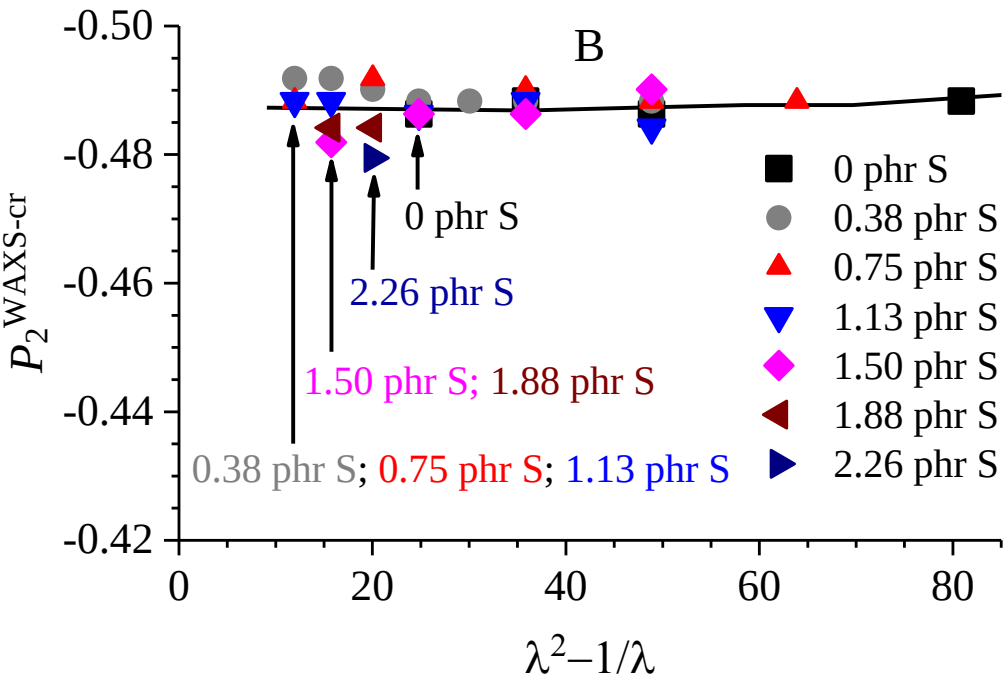

Fig. 9. Values of the order parameters for the amorphous $P_2^{WAXS-am}$ (A,A') and crystalline $P_2^{WAXS-cr}$ (B) segments as a function of the elongation parameter (λ^2-1/λ) of the HNBR samples with different crosslink densities. The dashed vertical bars in A and A' indicate the deformations of $\varepsilon = 200$ and 300%. The arrows in B mark the deformation of incipient crystallization. In A', data relative to the non-vulcanized sample HNBR-NV are evaluated from the azimuthal profiles extracted from the two-dimension WAXS fiber images of Fig. S8. Vulcanized samples were stretched at strain rate $v = 2$ min^{-1}, the non vulcanized sample (A') at strain rate $v = 10$ min^{-1}. The values of $P_2^{WAXS-am}$ are affected by 10% relative error.

The negative values of the order parameter $P_2^{WAXS-am}$ indicate that the amorphous segments tend to become oriented in the direction parallel to the chain axes already at low deformations (Fig. 9A,A'). It is apparent that the absolute values of the order parameter associated to the amorphous segments experience a steep increase at low deformations until reaching a quasi-plateau for values of (λ^2-1/λ) close to 10-20 (i.e. $\varepsilon \approx$200-300%) (Fig. 9A, A') and that the degree of orientation achieved by the amorphous segments at any deformation increases with increasing the crosslink density.

For all the samples, the plateau seems to be reached in correspondence of the deformation at incipient crystallization (200 to 300%, λ^2-1/λ comprised between 9 and 16). This indicates that when crystallization occurs, the orientation of the amorphous segments does not increase any longer with strain because crystallization leads to a partial relaxation of the amorphous chains linked to the crystallites, as predicted

by Flory's theory [14] and observed in vulcanized samples of natural rubber [24], [26], [27], [28], [29] and synthetic elastomers as polyisoprene, polybutadiene, and butyl rubber [21]. This confirms that SIC can be understood and described as a phase equilibrium [28].

On the basis of Equation 8, the initial slope of the order parameter versus (λ^2-1/λ) is expected to increase with increasing of ν_e (Fig. 9A,A'). However, due the lack of direct measurements at deformations lower than 100% (i.e. for λ^2-1/λ lower than 5), it is not possible to hazard any quantitative evaluation of this slope. Indirect information may be obtained from inspection of the dependence of the values of the order parameter achieved at 300% deformation (λ^2-1/λ = 15.75) ($P_2^{WAXS\text{-}am}$(300%)) on ν_e. The values of $P_2^{WAXS\text{-}am}$(300%) are reported in Fig. 10 as a function of ν_e, where they are compared with those of the order parameter occurring at the maximum deformation reached in the stretching experiments ($P_2^{WAXS\text{-}am}(\varepsilon_{max})$). It is apparent that whereas the values of $P_2^{WAXS\text{-}am}(\varepsilon_{max})$ is almost constant and equal to -0.029 regardless of crosslink density, the values of $P_2^{WAXS\text{-}am}$(300%) decrease with increasing ν_e. This suggests that the rate with which the amorphous segments become oriented parallel to the stretching direction tend to increase with increasing ν_e, but, once the deformation at crystallization onset is achieved, relaxation of the amorphous segments entails that the amorphous phase tends to reach the same degree of orientation regardless of crosslink density. The linear dependence of $P_2^{WAXS\text{-}am}$(300%) on ν_e. also suggests that even at zero crosslink density, the HNBR samples should approach a non-zero value of the order parameter close to -0.017, because of the presence of trapped entanglements. This value is close to the value of $P_2^{WAXS\text{-}am}$(300%) approached by the non-vulcanized sample (data not shown), even though such entanglements are effective to promote chain orientation at zero crosslink density only at fast enough deformation rates, as discussed before.

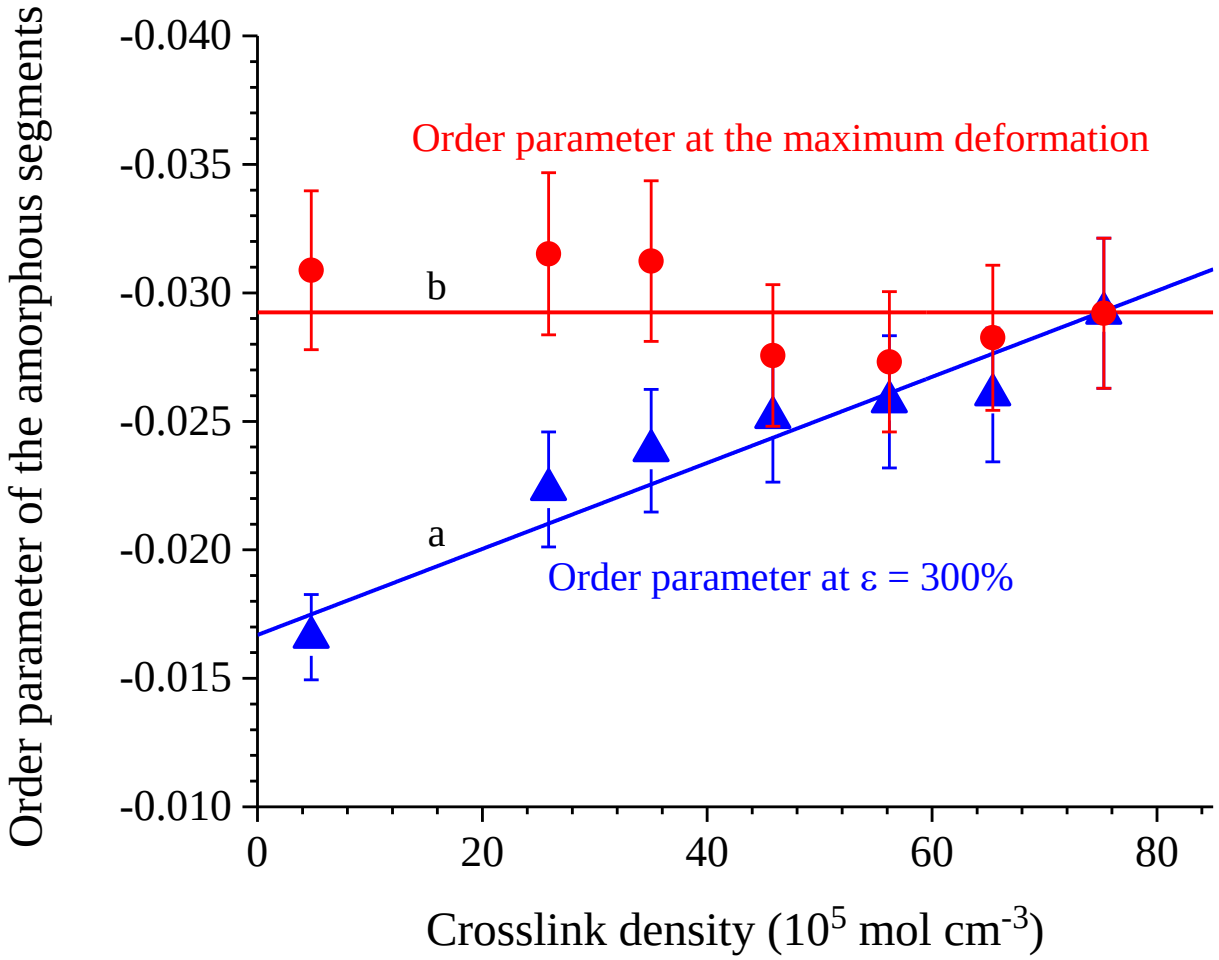

Fig. 10. Values of the order parameter $P_2^{WAXS\text{-}am}$ achieved by the amorphous segments at 300% deformation (λ^2-1/λ = 15.75) ($P_2^{WAXS\text{-}am}$(300%), (a) and at maximum deformation reached in the stretching experiments ($P_2^{WAXS\text{-}am}$(ε_{max}), (b), as a function of crosslink density of the vulcanized HNBR samples. The samples were stretched at strain rate v = 10 min^{-1}.

As far as the crystalline phase is concerned, it reaches a degree of orientation higher than the amorphous phase (Fig. 9B). In particular, the values of the order parameter $P_2^{WAXS\text{-}cr}$ is constant and close to -0.5, regardless of the deformation and the crosslink density. In Fig. 9B, the deformation marking the onset of crystallization is indicated by the vertical arrows for the different samples. These data confirm that the deformation at crystallization onset tends to increase with the increase of the crosslink density and it is around 200-250% for the samples HNBR-0.38, HNBR-0.75 and HNBR-1.1, with crosslink density of 4.8, 26 and 35 10^{-5} mol/cm^3 (λ^2-1/λ ≈ 12), 300% for the samples HNBR-1.5 and HNBR-1.9, with crosslink density of 46 and 56 10^{-5} mol/cm^3 (λ^2-1/λ ≈ 15), and around 350% for the samples HNBR-2.3, with crosslink density of 65 10^{-5} mol/cm^3 (λ^2-1/λ ≈ 20). The non-vulcanized sample HNRB-NV, instead, starts

crystallizing at 400% deformation (λ^2-1/$\lambda \approx 25$) provided that the deformation rate is fast enough to prevent the viscous flow of the chains. The fact that for the non-vulcanized sample the deformation at crystallization onset is the highest is due to the peculiar behavior of this sample. As stated above, the non-vulcanized sample undergoes SIC only if the strain rate is higher than a threshold, that is in conditions for which the crystallization rate becomes higher than the rate of segmental dynamics inducing relaxation of the amorphous chains. In other terms, the absence of topological constraints due to chemical crosslinks shifts the critical strain marking the SIC onset toward higher values because a higher stretching rate corresponds to a sort of an increase of the supercooling.

The values of the coefficient associated to the fourth Legendre polynomial $P_4^{\text{WAXS-x}}$ for the amorphous and crystalline phases are reported in Table S3. Values comprised in between -1 10^{-4} and 6 10^{-3} are obtained for the amorphous phase, whereas for the crystalline phase the values of $P_4^{\text{WAXS-cr}}$ are close to 0.375.

The degree of orientation achieved by the crystals by effect of SIC is also calculated extracting the values of the crystalline order parameter from the azimuthal intensity distribution of the meridional reflection at $2\theta(\text{MoK}\alpha) = 5.7°$ (Fig. S9). The so obtained values of $P_2^{\text{WAXS-cr-mer}}$ are reported in Fig. S12 as a function of (λ^2-1/λ). Values $P_2^{\text{WAXS-cr-mer}}$ around 0.90 (close to minus two times the values of $P_2^{\text{WAXS-cr}}$ of Fig. 9B [51]) are obtained regardless of crosslink density and deformation, confirming that well-oriented crystals are formed since the beginning of crystallization through SIC.

The above results indicate that, once the strain at incipient crystallization is reached, the formed crystallites are highly oriented with their chain axes parallel to the stretching direction and their alignment degree does not increase significantly by further stretching, neither with the increasing crosslink density. This is in agreement with the prediction of Flory theory[14] and suggests that the orientation achieved by the amorphous segments induce not only a high degree of orientation of the SIC crystals, but also a fast crystallization rate (Fig. 8B). The extension of the amorphous chains induces a decrease of the barrier for primary nucleation and crystal growth through the decrease of the entropy penalty for the incorporation

of chain segments into the crystallites (entropy barrier effect) [52]. The non-monotonous change of the maximum incremental crystallinity index with respect to the deformation $(dx_c/d\varepsilon)_{max}$ as a function of the crosslink density (Fig. 8B) may be due to a competition between the entropy barrier effect and the reduction in segmental mobility with increase of ν_e (dynamic effect). At low crosslink density, the degree of orientational order achieved by the amorphous segments is low. Consequently, the "SIC rate" is constant, because the dynamic effect prevails over the entropy barrier effect. However, with further increase of ν_e, the degree of orientation achieved by the amorphous segments increases above a threshold, inducing a neat decrease of the barrier for primary nucleation and crystal growth. Since the segmental mobility is reduced only a little, the entropy barrier effect becomes prevalent over the dynamic effect. It is expected that the dynamic effect would become again prevalent, for vulcanizates with very high crosslink densities. However, this expectation cannot be checked because the HNBR samples also become fragile and unable to crystallize by increasing ν_e, as shown by the highly crosslinked HNBR sample with ν_e equal to 75 10^{-5} mol cm^{-3} (added sulfur content 3.01 phr) that crystallizes only a little and breaks at deformations close to the deformation at incipient crystallization (300 to 350%, Fig. S10G, G', S11G).

As a further remark, it is worth pointing out that the high degree of orientation achieved by the crystals generated by SIC, along with the sigma-shaped increase of crystallinity with increasing deformation are both responsible for the high strain hardening shown by the weakly and medium crosslinked HNBR samples at high deformations (Fig. 3).

Conclusions

A study of the thermal and mechanical properties, the molecular chain orientation and SIC behavior of a HNBR sample with an ACN content of 44 wt% and a residual unsaturation content of 9 % as a function of crosslink densities is reported. The analysis is focused on specimens that have not been subjected to any prior deformation. The values of the glass transition temperature of the HNBR samples increase linearly with increasing crosslink density. The values of the Young's modulus of the vulcanized samples are three times higher than that of the non-vulcanized counterpart and tend to increase with increasing the

crosslink density. The main effect of vulcanization with increasing crosslink density is an increase of the mechanical strength and a decrease of ductility.

All HNBR samples with varying crosslink density are amorphous at *RT* and, above a critical value of deformation, show SIC, due to the crystallization of the alternating sequences of tetramethylene and ACN units (TMAC). The crystallinity index increases with the increase of deformation according to a sigmoidal shape, until reaching a maximum value either because it reaches a plateau, or because, at high crosslink density, the samples rupture. Furthermore, the deformation at SIC onset for the crosslinked samples tends to increase with increasing the crosslink density. One may speculate that this may be due to occurrence of irreversible transformations during the first hysteresis cycle of stretching and release of the tension coupled with the presence of possible crosslink heterogeneities.

The crystallization of the TMAC sequences is preceded by the orientation of the chain segments in the amorphous phase. The degree of orientation of the amorphous phase increases with increasing deformation until reaching a plateau at deformations close to that at incipient crystallization. The orientational order achieved by the crystals is much higher than that of the amorphous phase, remains constant with strain and does not depend on the crosslink density. These results indicate that the SIC behavior of the HNBR samples is similar to that of crosslinked NR, and in contrast with some of the predictions of the Flory and Sotta-Albouy theory [14], [28].

Specific descriptors are introduced to analyze the SIC behavior of the HNBR samples, namely maximum crystallinity achieved by stretching (x_c(max)) before breaking, the order parameter of the amorphous phase at 300% deformation ($P_2^{\text{WAXS-am}}$(300%)), and the incremental crystallinity index with respect to the deformation $(dx_c/d\varepsilon)_{max}$ ("SIC rate").

In particular, it is shown that the values of x_c(max) decrease almost linearly with increasing crosslink density ν_e, due to the disturbance effect exerted by the chemical crosslink that cause a shortening of the crystallizable sequence and a reduction of the segmental mobility in the amorphous phase. Extrapolation of x_c(max) *vs.* ν_e data allows to infer that for crosslink densities greater than a ν_e-threshold equal to ≈80 10^{-5} mol cm^{-3} crystallization does not occur anymore.

It is also shown that the orientational order achieved by the amorphous phase $P_2^{WAXS\text{-}am}(300\%)$ at 300% deformation increases almost linearly with the increasing crosslink density. This allows establishing that at zero crosslink density, the non-vulcanized HNBR sample is characterized by the presence of trapped entanglements that account for its SIC behavior, provided that the stretching at deformation above the critical values is fast enough to prevent irreversible segmental relaxation phenomena and viscous flow.

Finally, it is shown that the values of the "SIC rate" depend on the crosslink density in a non-monotonous way. It is argued that this complexity arises because, with the increasing crosslink density, two competing effects come into play, namely the decrease of entropy barriers for the primary nucleation and growth of the crystals and the simultaneous decrease of segmental mobility in the amorphous phase.

Data Availability

The data presented in this study are available on request from the corresponding authors.

Appendix A. Supplementary data

Supplementary data to this article can be found online.

References

[1] W. Obrecht, H. Buding, U. Eisele, Z. Szentivanyi, J. Thörmer, Hydrierter nitrilkautschuk ein werkstoff mit neuen eigenschaften, Angew. Makromol. Chem. 145 (1986) 161–179. https://doi.org/10.1002/apmc.1986.051450109

[2] H. Wang, L. Yang, G.L. Rempel, Homogeneous hydrogenation art of nitrile butadiene rubber: a review, Polym. Rev. 53 (2013,) 192-239. https://doi.org/10.1080/15583724.2013.776586

[3] C. Wrana, K. Reinartz, H.R. Winkelbach Therban® The High Performance Elastomer for the New Millennium, Macromol. Mater. Eng., 286 (2001) 657-662. https://doi.org/10.1002/1439-2054(20011101)286:11%3C657::AID-MAME657%3E3.0.CO;2-2

[4] S. Bhattacharjee, A.K. Bhowmick, B.N. Avasthi, Degradation of hydrogenated nitrile rubber, Polym. Degrad. Stabil. 31 (1991) 71–87. https://doi.org/10.1016/0141-3910(91)90097-B

[5] R.A. Chaudhry, I.A. Hussein, M.B. Amin, B.F. Abu Sharkh, Influence of molecular parameters and processing conditions on degradation of hydrogenated nitrile butadiene rubbers, J. Appl. Polym. Sci. 97 (2005) 1432–1441. https://doi.org/10.1002/app.21577

[6] J. Troufflarda, H. Laurenta, G. Rioa, B. Omnès, S. Javanaud, Temperature-dependent modelling of a HNBR O-ring seal above and below the glass transition temperature, Mater. Des. 156 (2018) 1–15. https://doi.org/10.1016/j.matdes.2018.06.016

[7] X. Chang, H. Yin, Y. Lyu, X. Shi, M. Hoch, HNBR-based composite for seals used in coolant fluids: swelling related to different silicates at high temperature, Polymer 178 (2019) 121691. https://doi.org/10.1016/j.polymer.2019.121691

[8] Hanbook of Synthetic Rubbers, M. van Duin, H. Dikland, T. Früh, T. Groß, C. Haßmann, N. Sary, R. Schmidt (Eds.) ARLANXEO Deutschland GmbH: Domagen (Germany), 2020.

[9] D. Braun, A. Haufe, D. Leiß, G.P. Hellmann, Strain-induced crystallization and miscibility behaviour of hydrogenated nitrile rubbers, Die Angew. Makromol. Chem. 202 (1992) 143-158. https://doi.org/10.1002/apmc.1992.052020109

[10] T. Kobatake, K. Kodama, S. Hayashi, A. Yoshioka, Improvement of low-temperature flexibility of hydrogenated nitrile-butadiene rubber. Rubber Chem. Technol. 70 (1997) 839-854. https://doi.org/10.5254/1.3538464

[11] X. Zhang, J. Wu, Z. Xu, D. Yue, S. Wu, S. Yan, Y. Lu, L. Zhang, Comparative study on the molecular chain orientation and strain-induced crystallization behaviors of HNBR with different acrylonitrile content under uniaxial stretching, Polymer 219 (2021) 123520. https://doi.org/10.1016/j.polymer.2021.123520

[12] N. Osaka, M. Kato, H. Saito, Mechanical properties and network structure of phenol resin crosslinked hydrogenated acrylonitrile-butadiene rubber, J. Appl. Polym. Sci. 129 (2013) 3396–3403. https://doi.org/10.1002/app.39010

[13] K. Narynbek Ulu, M. Dragicevic, P.-A. Albouy, B. Huneau, A.-S. Beranger, P. Heuillet, Strain-induced crystallization ability of hydrogenated nitrile butadiene rubber in Constitutive Models for Rubber X, CRC Press, London, ISBN 978-1-138-03001-5, 2017, p.279-282

[14] J.P. Flory, Thermodynamics of Crystallization in High Polymers. I. Crystallization Induced by Stretching, J. Chem. Phys. 15 (1947) 397–408. https://doi.org/10.1063/1.1746537

[15] A.N. Gent, Crystallization and the relaxation of stress in stretched natural rubber vulcanizates, Trans. Faraday Soc. 50 (1954) 521–533. https://doi.org/10.5254/1.3542793

[16] B. Huneau, Strain-Induced Crystallization of Natural Rubber: a Review of X-ray Diffraction Investigations, Rubber Chem. Tech. 84 (2011) 425–452. https://doi.org/10.5254/1.3601131

[17] M. Tosaka, S. Kohjiya, S. Murakami, S. Poompradub, Y. Ikeda, S. Toki, I. Sics, B.S. Hsiao, Effect of network-chain length on strain-induced crystallization of NR and IR vulcanizates, Rubber Chem. Tech. 77 (2004) 711–723. 23 https://doi.org/10.5254/1.3547846

[18] M. Tosaka, S. Murakami, S. Poompradub, S. Kohjiya, Orientation and Crystallization of Natural Rubber Network As Revealed by WAXD Using Synchrotron Radiation, Macromolecules 37 (2004) 3299–3309. 72 https://doi.org/10.1021/ma0355608

[19] M. Tosaka, Strain-Induced Crystallization of Crosslinked Natural Rubber as Revealed by X-ray Diffraction Using Synchrotron Radiation, Polymer J. 39 (2007) 1207–1220. 22 https://doi.org/10.1295/polymj.PJ2007059

[20] M. Tosaka, S. Kohjiya, Y. Ikeda, S. Toki, B.S. Hsiao, Molecular orientation and stress relaxation during strain-induced crystallization of vulcanized natural rubber, Polymer J. 42 (2010) 474–481. https://doi.org/10.1038/pj.2010.22

[21] S. Toki, I. Sics, B. S. Hsiao, S. Murakami, M. Tosaka, S. Poompradub, S. Kohjiya, Y. Ikeda, Structural Developments in Synthetic Rubbers during Uniaxial Deformation by In Situ Synchrotron X-Ray Diffraction. J. Polym. Sci.: Part B: Polym. Phys. 42, 956–964 (2004). https://doi.org/10.1002/polb.10679

[22] S.; Toki, I. Sics, S. Ran, L. Liu, B.S. Hsiao, S. Murakami, K. Senoo, S. Kohjiya, New Insights into Structural Development in Natural Rubber During Uniaxial Deformation by In Situ Synchrotron X-ray Diffraction, Macromolecules 35 (2002) 6578-6584 https://doi.org/10.1021/ma0205921

[23] S. Murakami, K. Senoo, S. Toki, S. Kohjiya, Structural development of natural rubber during uniaxial stretching by in situ wide angle X-ray diffraction using a synchrotron radiation, Polymer 43 (2002) 2117–2120. https://doi.org/10.1016/S0032-3861(01)00794-7

[24] M. Tosaka, A Route for the Thermodynamic Description of Strain-Induced Crystallization in Sulfur-Cured Natural Rubber, Macromolecules 42 (2009) 6166–6174. https://doi.org/10.1021/ma900954c

[25] S. Trabelsi, P.-A. Albouy, J. Rault, Crystallization and Melting Processes in Vulcanized Stretched Natural Rubber, Macromolecules 36 (2003) 7624–7639. 61 https://doi.org/10.1021/ma030224c

[26] P.A. Albouy, G. Guillier, D. Petermann, A. Vieyres, O. Sanseau, P. Sotta, A stroboscopic X-ray apparatus for the study of the kinetics of strain-induced crystallization in natural rubber, Polymer 53 (2012) 3313–3324. https://doi.org/10.1016/j.polymer.2012.05.042

[27] P.A. Albouy, P. Sotta, Draw Ratio at the Onset of Strain-Induced Crystallization in Cross-Linked Natural Rubber, Macromolecules 53 (2020) 992−1000. https://doi.org/10.1021/acs.macromol.9b01957.

[28] P. Sotta, P.A. Albouy, Strain-Induced Crystallization in Natural Rubber: Flory's Theory Revisited, Macromolecules 53 (2020) 3097–3109. https://doi.org/10.1021/acs.macromol.0c00515

[29] J. Rault, J. Marchal, P. Judeinstein, P.-A. Albouy, Stress-Induced Crystallization and Reinforcement in Filled Natural Rubbers: ^{2}H NMR Study, Macromolecules 39 (2006) 8356–8368. https://doi.org/10.1021/ma0608424

[30] P.-A. Albouy, A. Vieyres, R. Pérez-Aparicio, O. Sanséau, P. Sotta, The impact of strain-induced crystallization on strain during mechanical cycling of cross-linked natural rubber, Polymer 55 (2014) 4022-4031. https://doi.org/10.1016/j.polymer.2014.06.034

[31] A. Vieyres, R. Pérez-Aparicio, P.-A. Albouy, O. Sanseau, K. Saalwächter, D. R. Long, P. Sotta, Sulfur-Cured Natural Rubber Elastomer Networks: Correlating Cross-Link Density, Chain Orientation, and Mechanical Response by Combined Techniques, Macromolecules 46 (2013) 889–899. https://doi.org/10.1021/ma302563z

[32] J.-M. Chenal, L. Chazeau, L. Guy, Y. Bomal, C. Gauthier, Molecular weight between physical entanglements in natural rubber: A critical parameter during strain-induced crystallization, Polymer 48 (2007) 1042-1046. 84 https://doi.org/10.1016/j.polymer.2006.12.031

[33] J.-M. Chenal, C. Gauthier, L. Chazeau, L. Guy, Y. Bomal, Parameters governing strain induced crystallization in filled natural rubber, Polymer 48 (2007) 6893-6901. 63 https://doi.org/10.1016/j.polymer.2007.09.023

[34] Y. Ikeda, Y. Yasuda, K. Hijikata, M. Tosaka, S. Kohjiya, Comparative Study on Strain-Induced Crystallization Behavior of Peroxide Cross-Linked and Sulfur Cross-Linked Natural Rubber, Macromolecules 41 (2008) 5876-5884. https://doi.org/10.1021/ma800144u

[35] L. R. G. Treloar, The Physics of Rubber Elasticity Oxford University Press, Oxford, 1975.

[36] N. Candau, R. Laghmach, L. Chazeau, J.-M. Chenal, C. Gauthier, T. Biben, E. Munch, Strain-Induced Crystallization of Natural Rubber and Cross-Link Densities Heterogeneities, Macromolecules 47 (2014) 5815−5824. https://doi.org/10.1021/ma5006843

[37] J.L. Valentín, P. Psadas, A. Fernández-Torres, M.A. Malmierca, L. Gonzáles, W. Chassé, K. Saalwächter, Inhomogeneities and chain dynamics in diene rubbers vulcanized with different cure systems, Macromolecules 43 (2010) 4210–4222. https://doi.org/10.1021/ma1003437

[38] G. R. Mitchell, A wide-angle X-ray study of the development of molecular orientation in crosslinked natural rubber, Polymer 25 (1984) 1562–1572. https://doi.org/10.1016/0032-3861(84)90148-4

[39] P. J. Flory, Principles of Polymer Chemistry, Cornell University Press, Ithaca, NY, 1953, Chap. 13 (Eq, 38), p. 578.

[40] P. Sanprasert, N. Sombatsompop, P. Sae-oui, C. Sirisinha, Cotton fibers reinforcement of HNBR: Control of fiber alignment and its influence on properties of HNBR vulcanizates, J. Appl. Polym. Sci. 131 (2014) 41090. https://doi.org/10.1002/app.41090

[41] W. Smitthipong, M. Nardin, J. Schultz, K. Suchiva, Adhesion and self-adhesion of rubbers, crosslinked by electron beam irradiation, Int. J. Adhes. and Adhes. 27 (2007) 352-357. https://doi.org/10.1016/j.ijadhadh.2006.09.010

[42] https://www.esrf.fr/computing/scientific/FIT2D/

[43] H. D. Deas, The diffraction of X-rays by a random assemblage of molecules having partial alignment. Acta Cryst, 5 (1952) 542-546. https://doi.org/10.1107/S0365110X52001507

[44] G. R. Mitchell, A.H. Windle Conformational analysis of oriented non-crystalline polymers using wide angle X-ray scattering. Colloid & Polymer Sci. 260 (1982) 754-761. https://doi.org/10.1007/BF01452065

[45] B. Alcock, K. Olafsen, J. Huse, F. Grytten The low temperature crystallization of hydrogenated nitrile butadiene rubber (HNBR). Polymer Testing. 66 (2018) 228. https://doi.org/10.1016/j.polymertesting.2017.12.027.

[46] J.E.K. Schawe, C. Wrana, Competition between Structural Relaxation and Crystallization in the Glass Transition Range of Random Copolymers. Polymers, 12 (2020) 1778. https://doi.org/10.3390/polym12081778.

[47] T. G. Fox, Influence of diluent and of copolymer composition on the glass temperature of a polymer system, Bull. Am. Phys. Soc. 1 (1956) 123–125. https://cir.nii.ac.jp/crid/1570572699490512512

[48] M. Tosaka, Strain-Induced Crystallization of Crosslinked Natural Rubber As Revealed by X-ray Diffraction Using Synchrotron Radiation. Polym. J. 39 (2007) 1207–1220. https://doi.org/10.1295/polymj.PJ2007059

[49] P. Chen, J. Zhao, Y.- Lin, J. Chang, L. Meng, D. Wang, W. Chen, L. Chen, L. Li, In situ characterization of strain-induced crystallization of natural rubber by synchrotron radiation wide-angle X-ray diffraction: construction of a crystal network at low temperatures. Soft Matter 15 (2019) 734 - 743. https://doi.org/10.1039/C8SM02126K

[50] B. Erman, J.E. Mark, Structures and Properties of Rubberlike Networks; Oxford University Press: New York, NY, USA, 1997.

[51] L.E. Alexander, X Ray Diffraction Methods in Polymer Science. Krieger Pub Co, 1979.

[52] C. Zhang, C. Liu, L. Wang, Y. Zhao, G.Liu, D. Wang, Verification of thermodynamic theories of strain-induced polymer crystallization. Chem. Comm. 2022, 58, 286-289. https://doi.org/10.1039/D1CC04134G.